

## Review

# Self-Interaction-Free Time-Dependent Density Functional Theory for Nonperturbative Treatment of Orientation-Dependent Multiphoton Processes of Diatomic Molecular Systems in Intense Ultrashort Laser Fields

John Heslar,<sup>1,\*</sup> Dmitry A. Telnov,<sup>2,†</sup> and Shih-I Chu<sup>‡1,3,§</sup>

<sup>1</sup>*Center for Quantum Science and Engineering, Department of Physics,  
National Taiwan University, Taipei 10617, Taiwan*

<sup>2</sup>*Department of Physics, St. Petersburg State University, St. Petersburg 198504, Russia*

<sup>3</sup>*Department of Chemistry, University of Kansas, Lawrence, Kansas 66045, USA*

(Received August 29, 2013)

We present a brief account of several recent *ab initio* nonperturbative studies of very-high-order nonlinear optical processes of diatomic molecular systems in intense ultrashort laser fields with arbitrary molecular orientation. We discuss some recent development of the *self-interaction-free* time-dependent density functional theoretical (TDDFT) methods with correct long-range asymptotic behavior. The time-dependent Kohn-Sham equations are accurately and efficiently treated by means of the time-dependent generalized pseudospectral (TDGPS) methods in space and time. The procedures are applied to the comprehensive investigation of the multiphoton ionization (MPI) and high-order harmonic generation (HHG) processes of homonuclear ( $H_2$ ,  $N_2$ , and  $F_2$ ) and heteronuclear (CO, BF, and HF) diatomic molecules in the presence of intense ultrashort laser pulses. Novel high-order nonlinear optical behavior including the electron correlation, multi-orbital effects, orientation-dependence, wavelet time-frequency spectra, and the interfacing of electronic structure with multiphoton dynamics, etc., are presented and discussed in details.

DOI: 10.6122/CJP.52.578

PACS numbers: 33.80.Rv, 42.65.Ky, 31.15.E-, 31.15.A-

## I. INTRODUCTION

The study of attosecond physics in intense ultrashort laser fields is a forefront subject of much current significance in ultrafast science and technology. Attosecond pulses can be produced by means of high harmonic generation (HHG) of atoms in intense laser fields [1–7] and the time profile of the attosecond pulses can be controlled by tuning the carrier envelope phase [8]. Recent progress of attosecond physics includes control of electron wave packets [9], probing of nuclear dynamics [10] and electronic dynamics [11], attosecond time-resolved spectroscopy [12], tomographic imaging of molecular orbitals [13], etc. One of the most novel features in an attosecond time scale is the real time observation of the motion of

<sup>‡</sup> Corresponding author

\*Electronic address: john.heslar@gmail.com

†Electronic address: telnov@pcqnt1.phys.spbu.ru

§Electronic address: sichu@ku.edu

electrons in atoms and molecules [14]. The generation of ever shorter attosecond pulses has continued to attract much interest and has become one of the most active research directions in attosecond metrology today. In this connection, we note that ultrahigh harmonics, up to orders greater than 5,000, have been recently realized experimentally [15].

A major role for theory in attosecond ultrafast science is to elucidate novel ways to investigate and to control electronic and other processes in matter on attosecond time scales. Strong-field multiphoton dynamics is central to many extreme nonlinear optical processes such as high-order harmonic generation (HHG), multiphoton ionization (MPI), above-threshold ionization (ATI), and attosecond pulse generation, etc. Fully *ab initio* non-perturbative treatment of many-electron quantum systems in strong fields in full dimensionality is a formidable task beyond the capability of current computational technology for the number of electrons  $N > 2$ . Even for the two-electron systems ( $N = 2$ ) with 6 spatial dimensions, accurate solution of the time-dependent Schrödinger equation (TDSE) is still a challenging and hot topic in atomic, molecular, and optical (AMO) physics today.

Due to the complexity of the time-dependent dynamics of *many-electron* quantum systems in intense laser pulses, most of our understanding of the strong-field multiphoton dynamics is based on approximate models, such as Keldysh-Faisal-Reiss (KFR) model [16–18], Ammosov-Delone-Krainov (ADK) model [19, 20]), strong-field approximation (SFA), and single-active-electron (SAE) model [21], etc. The SAE method has been successfully used for explaining several important aspects of HHG and ATI phenomena of rare gas atoms in linearly polarized laser fields in weak to medium-strong laser fields [21, 22]. However, the SAE and other approximate models can fail completely to explain experimental observations in strong fields.

There is currently a great demand and grand challenge to develop accurate theoretical formulations and precision computational methods for reliable nonperturbative treatment of ultrafast strong-field AMO physics, taking into account the electron structure and electron correlations. In this article, we focus on some of the recent developments and applications of the *self-interaction-free* time-dependent density functional theory (TDDFT) for the *ab initio* nonperturbative treatment of MPI and HHG processes in intense ultrashort laser fields.

The density functional theory (DFT), based on the fundamental work of Hohenberg and Kohn [23] and Kohn and Sham [24], has been widely used for the calculation of *ground-state* electronic structure of many-electron atoms, molecules, and solids in recent decades. DFT is a many-body theory in terms of the electron density  $\rho(\mathbf{r})$ . It provides a powerful alternative to *ab initio* wave function approach since the electron density  $\rho(\mathbf{r})$  possesses only three spatial dimensions no matter how large the system is. DFT proves accurate and computationally much less expensive than usual *ab initio* wave function methods and this accounts for its great success. However, the universal exchange-correlation (xc) energy functional form, which is a functional of the total electron density and the central ingredient of DFT, is not known exactly, and thus approximate xc energy functionals must be used. Due to the existence of the spurious *self-interaction energy* in the commonly used local spin density approximation (LSDA) [25] or the more refined generalized gradient approximation (GGA) [25–29] the corresponding xc potentials either decay exponentially and/or do not

have the correct long-range Coulombic ( $-1/r$ ) behavior. As such, the excited-state and ionization potential properties of conventional DFT calculations are not as reliable as those of the ground state. For example, the ionization potentials calculated by the LSDA or GGA energy functionals are typically 30 to 50% too low. It is clear that for proper TDDFT description of atomic and molecular dynamics, including multiphoton excitation, ionization, dissociation, and HHG processes, etc., the deficiency of self-interaction energy and long-range potential in the conventional steady-state DFT must be addressed first.

To advance the field in this direction, we have previously presented a *self-interaction-free* DFT for accurate treatment of excited states, autoionizing resonances, and ionization potentials of atoms [30, 31]. The method is based on the extension of the optimized effective potential (OEP) formalism [32, 33], the Krieger-Li-Iafrate (KLI) semi-analytical solution [34, 35] of the OEP, and the implementation of an explicit self-interaction-correction (SIC) term [31]. The OEP formalism is a rigorous many-body theory which takes as a starting point a given expression for the total energy  $E[\Psi_1\Psi_2\Psi_3...\Psi_N]$  for an N-electron system as a functional of a set of single-particle orbitals. Then the variationally best local effective potential is determined in such a way that when it is inserted in a stationary single-particle Schrödinger equation, it yields a set of N-eigenfunctions (corresponding to the N lowest energies) that minimize  $E[\Psi_1\Psi_2\Psi_3...\Psi_N]$ . In practice, the full OEP scheme is computationally rather formidable but the KLI semianalytical approach [34, 35] to the solution of OEP makes the computational scheme feasible. However, the KLI method [34–36] still requires the use of the *nonlocal* Hartree-Fock (HF) energy functionals in the construction of OEP. As shown in our previous work [31], the proposed OEP/KLI-SIC procedure uses only orbital-independent single-particle *local* potentials and is thus computationally more efficient than the KLI method [34, 35] but maintains similar accuracy. Further, the OEP so constructed is self-interaction-free and has the correct long-range ( $-1/r$ ) potential [31]. The binding energies of the highest occupied spin-orbitals also provide an excellent approximation to the ionization potentials of atoms (to within 1-5% of the experimental values) [37]. Furthermore, the OEP/KLI-SIC procedure also allows accurate description of the photoabsorption of autoionizing resonances within DFT for the first time [31] in good agreement with experimental data [38, 39]. Then the OEP/KLI-SIC procedure is further extended to the relativistic domain [40]. The theory is applied to the calculation of ground-state properties of atoms with  $Z = 2$  to 106 [40]. It is found that the ionization potentials (obtained from the highest occupied orbital energies) determined by the present relativistic OEP/KLI-SIC method [40] agree well with the experimental data [41] to within a few percent across the periodic table. To our knowledge this is the first DFT atomic-structure calculation that has achieved such a quantitative accuracy. These initial studies indicate that DFT with OEP/SIC can now be refined to the level that is capable of providing quantitative prediction of both static and dynamical properties of many-electron atomic systems.

To study the multiphoton processes of atomic systems in strong fields, we have developed a *self-interaction-free* time-dependent density functional theory (TDDFT) by extending the static OEP/KLI-SIC approach to the time domain [42], taking into account the proper long-range potential behavior. Similar to the static case [31], our TD-OEP/KLI-

SIC method [42] uses only *local* potential in the construction of (orbital-independent) OEP and is thus computationally more efficient. To solve the TD-OEP/KLI-SIC equations, we extend the time-dependent generalized pseudospectral (TDGPS) method [43] for *nonuniform* and optimal spatial grid discretization, allowing accurate and efficient solution of the time-dependent wave functions of many-electron atomic systems. The TD-OEP/KLI-SIC method has been applied successfully to the study of MPI/HHG processes of He [42] and heavier rare gas atoms [44] in intense laser pulses, as well as for the recent exploration of the frequency comb structure and coherence of rare gas atoms in the vuv-xuv regimes via HHG [45].

More recently, we have extended the self-interaction-free TDDFT to the diatomic molecular systems [30, 46, 47]. For the diatomic molecular systems, we used the prolate spheroidal coordinates, and a generalized pseudospectral (GPS) procedure is developed for nonuniform and optimal spatial discretization of the two-center Hamiltonian systems. High-precision molecular electronic structure information can be obtained by the use of only a modest number of grid points. Further extension of the TDDFT approach to the accurate study of MPI processes of triatomic molecular systems ( $\text{CO}_2$  and  $\text{H}_2\text{O}$ ) have been recently carried out by means of the time-dependent Voronoi-cell finite difference (VFD) method [48, 49].

This paper is organized as follows. In Sec. II, we describe the TDDFT approaches for the treatment of multiphoton processes in diatomic molecules. In Sec. III, we present the results for MPI and HHG studies of oriented  $\text{H}_2$  molecules. In Sec. IV, we analyze multiple orbital contributions to the MPI and HHG processes of homonuclear and heteronuclear diatomic molecules in intense ultrashort laser fields. We identify the patterns of constructive and destructive interference in the high-order harmonics for  $\text{F}_2$ ,  $\text{N}_2$ ,  $\text{CO}$ ,  $\text{BF}$ , and  $\text{HF}$  diatomic molecules. In Sec. V, we study orientation-dependent MPI and HHG of  $\text{N}_2$  and  $\text{F}_2$  molecules. We also investigate the high-order harmonic generation of aligned  $\text{CO}$  molecules. Section VI contains concluding remarks. Atomic units are used throughout the paper unless specified explicitly.

## II. TDDFT APPROACH WITH PROPER LONG-RANGE POTENTIAL FOR THE TREATMENT OF MULTIPHOTON PROCESSES OF DIATOMIC MOLECULES

In this section, we extend the time-dependent density functional theory (TDDFT) for the nonperturbative treatment of multiphoton processes of diatomic molecular systems in the presence of intense ultrashort laser pulses. Consider the solution of the time-dependent Kohn-Sham (TDKS) equations. In the spin-polarized theory, the spin-orbitals  $\psi_{n\sigma}(\mathbf{r}, t)$  corresponding to different spin projections  $\sigma$  satisfy the equations with different effective potentials  $v_{\text{eff},\sigma}(\mathbf{r}, t)$ :

$$i\frac{\partial}{\partial t}\psi_{n\sigma}(\mathbf{r}, t) = \left[-\frac{1}{2}\nabla^2 + v_{\text{eff},\sigma}(\mathbf{r}, t)\right]\psi_{n\sigma}(\mathbf{r}, t), \quad n = 1, 2, \dots, N_\sigma, \quad (1)$$

where  $N_\sigma$  ( $= N_\uparrow$  or  $N_\downarrow$ ) is the total number of electrons for a given spin  $\sigma$ . The total number of electrons in the system is  $N = \sum_\sigma N_\sigma$ . Within the single determinant approximation, the total  $N$ -electron wave function of the Kohn-Sham non-interacting system can be expressed as follows:

$$\Psi(t) = \frac{1}{\sqrt{N!}} \det[\psi_1 \cdot \psi_2 \cdots \psi_N]. \quad (2)$$

The electron spin-orbital densities  $\rho_{i\sigma}(\mathbf{r}, t)$  are determined by the occupied single-electron Kohn-Sham spin orbitals:

$$\rho_{i\sigma}(\mathbf{r}, t) = |\psi_{i\sigma}(\mathbf{r}, t)|^2. \quad (3)$$

Then the spin densities  $\rho_\sigma(\mathbf{r}, t)$  [ $= \rho_\uparrow(\mathbf{r}, t)$  or  $\rho_\downarrow(\mathbf{r}, t)$ ] are calculated as

$$\rho_\sigma(\mathbf{r}, t) = \sum_{i=1}^{N_\sigma} \rho_{i\sigma}(\mathbf{r}, t), \quad (4)$$

and the total electron density is a sum of the spin densities:

$$\rho(\mathbf{r}, t) = \sum_\sigma \rho_\sigma(\mathbf{r}, t). \quad (5)$$

The time-dependent effective potential  $v_{\text{eff},\sigma}(\mathbf{r}, t)$  is a functional of both electron spin densities  $\rho_\uparrow(\mathbf{r}, t)$  and  $\rho_\downarrow(\mathbf{r}, t)$ . The potential  $v_{\text{eff},\sigma}(\mathbf{r}, t)$  can be written in the general form

$$v_{\text{eff},\sigma}(\mathbf{r}, t) = v_n(\mathbf{r}) + v_H(\mathbf{r}, t) + v_{\text{xc},\sigma}(\mathbf{r}, t) + v_{\text{ext}}(\mathbf{r}, t) \quad (6)$$

where  $v_n(\mathbf{r})$  is the electron interaction with the nuclei,

$$v_n(\mathbf{r}) = -\frac{Z_1}{|\mathbf{R}_1 - \mathbf{r}|} - \frac{Z_2}{|\mathbf{R}_2 - \mathbf{r}|} \quad (7)$$

with  $Z_1$  and  $Z_2$  being the charges of the nuclei, and  $\mathbf{R}_1$  and  $\mathbf{R}_2$  being the positions of the nuclei (which are assumed to be fixed at their equilibrium positions);  $v_H(\mathbf{r}, t)$  is the Hartree potential due to electron-electron Coulomb interaction,

$$v_H(\mathbf{r}, t) = \int d^3r' \frac{\rho(\mathbf{r}', t)}{|\mathbf{r} - \mathbf{r}'|}. \quad (8)$$

The potential  $v_{\text{ext}}(\mathbf{r}, t)$  in Eq. (6) describes the interaction with the laser field. Using the dipole approximation and the length gauge, it can be expressed as follows:

$$v_{\text{ext}}(\mathbf{r}, t) = (\mathbf{F}(t) \cdot \mathbf{r}). \quad (9)$$

Here  $\mathbf{F}(t)$  is the electric field strength of the laser field, and the linear polarization is assumed. For the laser pulses with the sine-squared envelope, one has:

$$\mathbf{F}(t) = \mathbf{F}_0 \sin^2 \frac{\pi t}{T} \sin \omega_0 t \quad (10)$$

where  $T$  and  $\omega_0$  denote the pulse duration and the carrier frequency, respectively;  $F_0$  is the peak field strength.

The wave functions and operators are discretized with the help of the generalized pseudospectral (GPS) method in prolate spheroidal coordinates [46, 50–52]. The prolate spheroidal coordinates  $\xi$ ,  $\eta$ , and  $\varphi$  are related to the Cartesian coordinates  $x$ ,  $y$ , and  $z$  as follows [53]:

$$\begin{aligned} x &= a\sqrt{(\xi^2 - 1)(1 - \eta^2)} \cos \varphi, \\ y &= a\sqrt{(\xi^2 - 1)(1 - \eta^2)} \sin \varphi, \\ z &= a\xi\eta \quad (1 \leq \xi < \infty, \quad -1 \leq \eta \leq 1). \end{aligned} \quad (11)$$

In Eq. (11), we assume that the molecular axis is directed along the  $z$  axis, and the nuclei are located on this axis at the positions  $-a$  and  $a$ , so the internuclear separation  $R = 2a$ . For the unperturbed molecule, the projection  $m$  of the angular momentum onto the molecular axis is conserved, and the *exact* spin orbitals have factors  $(\xi^2 - 1)^{|m|/2}(1 - \eta^2)^{|m|/2}$  which are non-analytical at nuclei for odd  $|m|$ . Straightforward numerical differentiation of such functions could result in significant loss of accuracy. Therefore different forms of the kinetic energy operators have been suggested for even and odd  $m$  [50, 54]. However, for the molecules in the linearly polarized laser field with arbitrary orientations of the molecular axis, the projection of the electron angular momentum onto the molecular axis is not conserved any longer. In this case, we apply a full 3D discretization with respect to the coordinates  $\xi$ ,  $\eta$ , and  $\varphi$ . For  $\xi$  and  $\eta$ , we use the GPS discretization with non-uniform distribution of the grid points; for  $\varphi$ , the Fourier grid (FG) method [55] with uniform spacing of the grid points is more appropriate. To take care of the possible singularities at the nuclei, we use special mapping transformations of the coordinates  $\xi$  and  $\eta$  [56] which make the wave functions analytic at the nuclei for both even and odd projections of the angular momentum. The discretized kinetic energy operator takes the form of the matrix  $T_{ijk;i'j'k'}$ :

$$T_{ijk;i'j'k'} = \frac{1}{2a^2} \left[ \frac{T_{ii'}^{(\xi)} \delta_{jj'} + T_{jj'}^{(\eta)} \delta_{ii'}}{\sqrt{(\xi_i^2 - \eta_j^2)(\xi_{i'}^2 - \eta_{j'}^2)}} \delta_{kk'} + \frac{T_{kk'}^{(\varphi)} \delta_{ii'} \delta_{jj'}}{(\xi_i^2 - 1)(1 - \eta_j^2)} \right] \quad (12)$$

where the partial matrices  $T_{ii'}^{(\xi)}$ ,  $T_{jj'}^{(\eta)}$ , and  $T_{kk'}^{(\varphi)}$  related to the coordinates  $\xi$ ,  $\eta$ , and  $\varphi$ , respectively, have quite simple expressions [56]. The GPS method allows to achieve a high precision when using only a moderate number of grid points. For example, in the calculations of the unperturbed bound state energies of the hydrogen molecular ion, we used the kinetic energy matrices with only 72 grid points for  $\xi$  and 24 grid points for  $\eta$  (the  $\varphi$  angle is irrelevant in this case) and obtained the energies of the first several bound states very high accuracy; the computation time did not exceed a few minutes [57]. Table I shows the first 12 fully converged eigen-energies with 28 accurate digits.

The time-dependent Kohn-Sham equations (1) for two-center diatomic molecular systems are expressed in terms of prolate spheroidal coordinates and solved accurately and efficiently by means of the time-dependent generalized pseudospectral (TDGPS) method

TABLE I: High-precision bound state energies of  $\text{H}_2^+$  at internuclear separation 2 a.u.

State	Energy (a. u.)
$1\sigma_g$	-1.102634214494946461508968945
$1\sigma_u$	-0.6675343922023829303619702115
$1\pi_u$	-0.4287718198958564363139600911
$2\sigma_g$	-0.3608648753395038450386997512
$2\sigma_u$	-0.2554131650864845614172502361
$3\sigma_g$	-0.2357776288255547907092435479
$1\pi_g$	-0.2266996266436576389675221554
$1\delta_g$	-0.2127326818107631498576063244
$2\pi_u$	-0.2008648299115413183937711539
$4\sigma_g$	-0.1776810451262412913662883797
$3\sigma_u$	-0.1373129242771578364852227973
$5\sigma_g$	-0.1307918776321809748361441234

[46, 50, 51, 58]. The procedure consists of the following two steps: First a generalized pseudospectral (GPS) method is developed for nonuniform and optimal spatial discretization of the two-center Hamiltonian systems. Second, the TDKS equations are propagated in space and time by means of the split-operator method in the energy representation with spectral expansion of the propagator matrices. We employ the following split-operator, second-order short-time propagation formula:

$$\begin{aligned} \psi_{n\sigma}(\mathbf{r}, t + \Delta t) = & \exp\left(-\frac{i}{2}\Delta t \hat{H}_0\right) \exp\left(-i\Delta t V(\mathbf{r}, t + \frac{1}{2}\Delta t)\right) \\ & \times \exp\left(-\frac{i}{2}\Delta t \hat{H}_0\right) \psi_{n\sigma}(\mathbf{r}, t) + O((\Delta t)^3). \end{aligned} \quad (13)$$

Here  $\Delta t$  is the time propagation step,  $\hat{H}_0$  is the unperturbed electronic Hamiltonian which includes the kinetic energy and the effective potential before the laser field switched on,

$$\hat{H}_0 = -\frac{1}{2}\nabla^2 + v_{\text{eff},\sigma}(\mathbf{r}, 0). \quad (14)$$

The potential  $V(\mathbf{r}, t)$  describes the interaction with the laser field and can be expressed as follows:

$$V(\mathbf{r}, t) = v_{\text{eff},\sigma}(\mathbf{r}, t) - v_{\text{eff},\sigma}(\mathbf{r}, 0). \quad (15)$$

It contains the direct interaction with the field  $v_{\text{ext}}(\mathbf{r}, t)$  (9) as well as terms due to the variation of the density. For the field polarized under the angle  $\gamma$  with respect to the molecular axis, the direct interaction can be expressed as follows, using the prolate spheroidal coordinates:

$$v_{\text{ext}}(\xi, \eta, \varphi, t) = aF(t) \left( \xi\eta \cos \gamma + \sqrt{(\xi^2 - 1)(1 - \eta^2)} \cos \varphi \sin \gamma \right). \quad (16)$$

Note that Eq. (13) is different from the conventional split-operator techniques [59, 60], where  $\hat{H}_0$  is usually chosen to be the kinetic energy operator and  $\hat{V}$  the remaining Hamiltonian depending on the spatial coordinates only. The use of the *energy*-representation in Eq. (13) allows the explicit *elimination* of the undesirable fast-oscillating *high-energy* components and speeds up considerably the time propagation [43, 46, 58]. For the given  $\Delta t$ , the propagator matrix  $\exp\left(-\frac{i}{2}\Delta t \hat{H}_0\right)$  is time-independent and constructed only once from the spectral expansion of the unperturbed Hamiltonian  $\hat{H}_0$  before the propagation process starts. The matrix  $\exp\left(-i\Delta t V(\mathbf{r}, t + \frac{1}{2}\Delta t)\right)$  is time-dependent and must be calculated at each time step. However, for interaction with the laser field in the length gauge, this matrix is diagonal (as any multiplication by the function of the coordinates in the GPS and FG methods), and its calculation is not time-consuming.

### III. MULTIPHOTON IONIZATION AND HIGH-ORDER HARMONIC GENERATION OF ORIENTED H<sub>2</sub> MOLECULES

The exact form of the exchange-correlation (xc) potential  $v_{\text{xc},\sigma}(\mathbf{r}, t)$  is unknown. However, high-quality approximations to the xc potential are becoming available. When these potentials, determined by time-independent ground-state DFT, are used along with TDDFT in the electronic structure calculations, both inner shell and excited states can be calculated rather accurately [61]. In the time-dependent calculations, we adopt the commonly used adiabatic approximation, where the xc potential is calculated with the time-dependent density. The adiabatic approximation had recently many successful applications to atomic and molecular processes in intense external fields [30, 61]. Previously we have developed a *self-interaction-free* TDDFT approach for the treatment of MPI and HHG of H<sub>2</sub> diatomic molecules [46] by means of the TD-OEP/KLI-SIC formalism. The resulting equations are structurally similar to the time-dependent Hartree-Fock equations, but include the many-body effects through an orbital independent single-particle local time-dependent xc potential. A numerical time-propagation technique is introduced for accurate and efficient solution of the TDDFT/OEP-SIC equations for two-center diatomic molecular systems. This procedure involves the use of a generalized pseudospectral method for *nonuniform* optimal grid discretization of the Hamiltonian in prolate spheroidal coordinates and a split-operator scheme in the energy representation for the time development of the electron orbital wave functions. High-precision time-dependent wave functions can be obtained by this procedure with the use of only a modest number of spatial grid points. Particular attention is paid to the exploration of the spectral and temporal structures of HHG by means of the wavelet



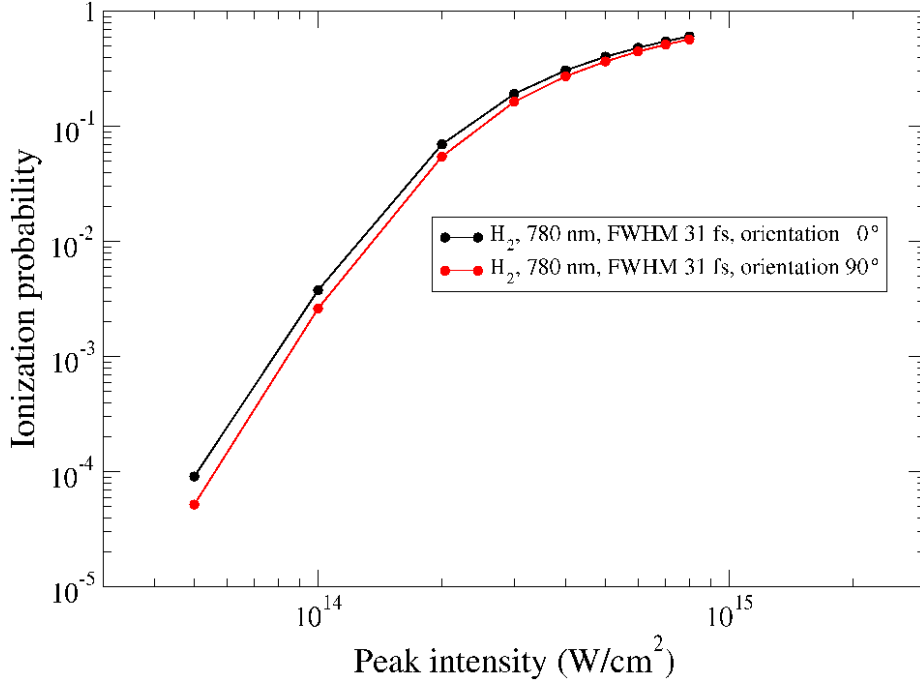


FIG. 1: MPI probabilities of H<sub>2</sub> molecule for the parallel and perpendicular orientation as a function of the peak intensity of the laser field.

time-frequency analysis. The results reveal striking details of the spectral and temporal fine structures of HHG, providing new insights regarding the detailed HHG mechanisms in different energy regimes.

For our more recent study of the MPI and HHG processes of H<sub>2</sub> molecules, we use the LB94 (van Leeuwen – Baerends) xc potential [62]:

$$v_{xc,\sigma}^{\text{LB94}}(\mathbf{r}, t) = v_{x,\sigma}^{\text{LSDA}}(\mathbf{r}, t) + v_{c,\sigma}^{\text{LSDA}}(\mathbf{r}, t) - \frac{\beta x_{\sigma}^2(\mathbf{r}, t) \rho_{\sigma}^{1/3}(\mathbf{r}, t)}{1 + 3\beta x_{\sigma}(\mathbf{r}, t) \ln\{x_{\sigma}(\mathbf{r}, t) + [x_{\sigma}^2(\mathbf{r}, t) + 1]^{1/2}\}}. \quad (17)$$

The LB94 potential contains a parameter  $\beta$ , which has been adjusted in time-independent DFT calculations of atomic and molecular systems and has the value  $\beta = 0.05$  [62]. The first two terms in Eq. (17),  $v_{x,\sigma}^{\text{LSDA}}$  and  $v_{c,\sigma}^{\text{LSDA}}$  are the exchange and correlation potentials within the local spin density approximation (LSDA). The last term in Eq. (17) is the gradient correction with  $x_{\sigma}(\mathbf{r}) = |\nabla \rho_{\sigma}(\mathbf{r})|/\rho_{\sigma}^{4/3}(\mathbf{r})$ , which ensures the proper long-range asymptotic behavior  $v_{xc,\sigma}^{\text{LB94}} \rightarrow -1/r$  as  $r \rightarrow \infty$ . The correct long-range asymptotic behavior of the LB94 potential allows to reproduce the orbital energy of H<sub>2</sub> with high accuracy (15.3 eV, that is within 1% of the exact ionization energy of 15.426 eV [63]; the internuclear separation is set to the experimental value of 1.4 a. u. [63].)

We have performed calculations of MPI probabilities and HHG spectra of H<sub>2</sub> molecules for the parallel and perpendicular orientations with respect to the polarization of

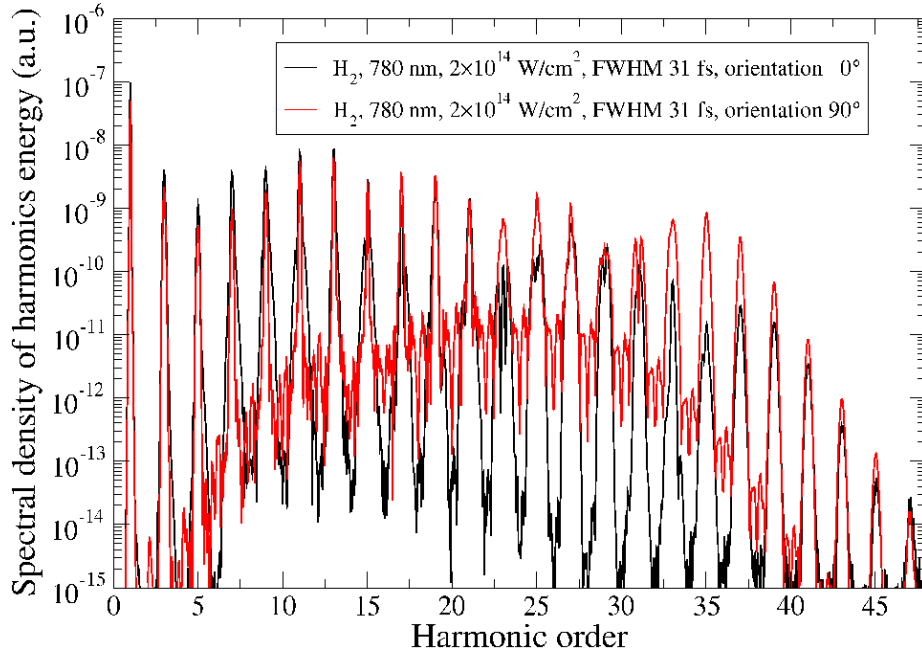


FIG. 2: HHG spectra of  $H_2$  molecule for the parallel and perpendicular orientation at the peak intensity of the laser field  $2 \times 10^{14} \text{ W/cm}^2$ .

the laser field. The carrier wavelength is 780 nm, the laser pulse has a sine-squared envelope with 24 optical cycles (full width at half maximum is 31 fs). The intensity-dependent MPI probabilities are shown in Fig. 1. As one can see, the results for the parallel and perpendicular orientations do not differ much and become closer as the peak intensity of the laser field increases. A weak orientation dependence of the MPI probability can be explained by the properties of the electron density distribution in the unperturbed  $H_2$  molecule which possesses only a weak anisotropy. The latter is due to the short internuclear distance,  $\sigma_g$  symmetry of the electronic orbital, and moderate ionization potential which makes the density distribution spread over larger space domain.

In Figs. 2 and 3, we show the spectral density of the harmonic radiation energy at the peak intensities of the laser field  $2 \times 10^{14} \text{ W/cm}^2$  and  $3 \times 10^{14} \text{ W/cm}^2$ . Again, the HHG spectra corresponding to the parallel and perpendicular orientation look similar. One can notice, however, a minimum in the vicinity of the 35th harmonic which is present for the parallel orientation only. The existence of this minimum can be attributed to destructive two-center interference [64] during the recombination stage of the HHG process [65]. Destructive interference is possible at the parallel orientation for some kinetic energy of the recombining electron, depending on the internuclear separation [64], while at the perpendicular orientation the contributions from the two centers in  $H_2$  to the harmonic signal always interfere constructively.

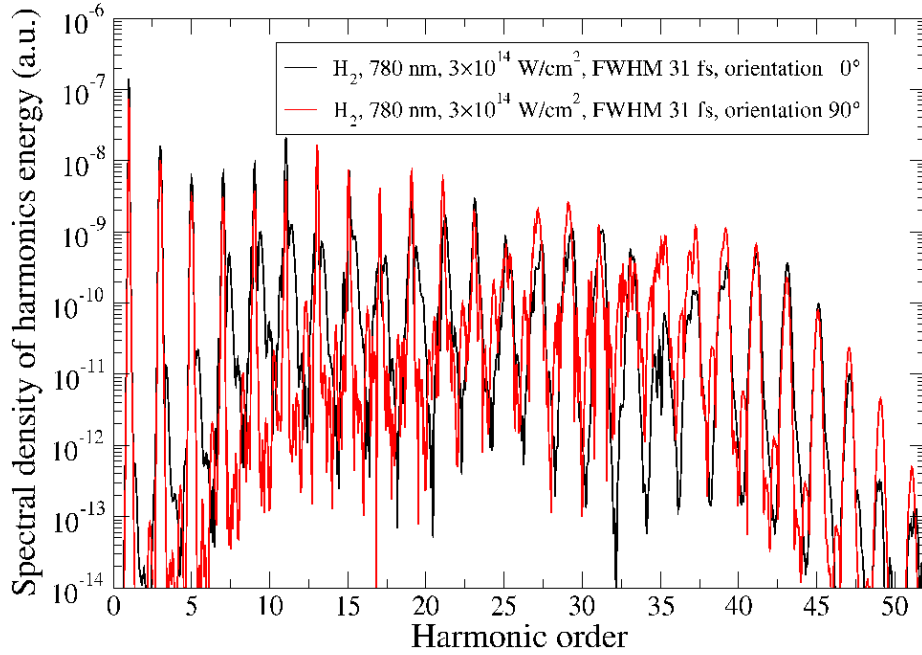


FIG. 3: HHG spectra of  $H_2$  molecule for the parallel and perpendicular orientation at the peak intensity of the laser field  $3 \times 10^{14} \text{ W/cm}^2$ .

#### IV. MULTIPHOTON IONIZATION AND HIGH-ORDER HARMONIC GENERATION OF HETERONUCLEAR AND HOMONUCLEAR DIATOMIC MOLECULES IN INTENSE ULTRASHORT LASER FIELDS: AN ALL-ELECTRON TDDFT STUDY

##### IV-1. Multiphoton Ionization of Heteronuclear and Homonuclear Diatomic Molecular Systems

In this section, we present all-electron TDDFT calculations of the MPI of  $N_2$  and  $CO$  diatomic molecules [47]. The ground-state electronic configurations is  $1\sigma_g^2 1\sigma_u^2 2\sigma_g^2 2\sigma_u^2 1\pi_u^4 3\sigma_g^2$  for  $N_2$  and  $1\sigma^2 2\sigma^2 3\sigma^2 4\sigma^2 1\pi^4 5\sigma^2$  for  $CO$ , respectively.  $N_2$  and  $CO$  are isoelectronic molecules, both having 14 electrons and triple bonds. Since the  $CO$  molecule has unequal nuclear charges, its ground electronic state possesses a permanent dipole moment, calculated here to be 0.149 Debye. The corresponding experimental value is 0.112 Debye [66]. Furthermore, there is no concept of gerade and ungerade orbitals for  $CO$  (or any other heteronuclear diatomic molecule) since the inversion symmetry of the potential is broken. For the studies of the diatomic molecules, we utilize the modified van Leeuwen – Baerends

TABLE II: Comparison of the field-free molecular orbital energy levels of CO and N<sub>2</sub>, calculated with the LB $\alpha$  potential, and the experimental ionization potentials (in a.u.).

CO						
Orbital	1 $\sigma$	2 $\sigma$	3 $\sigma$	4 $\sigma$	1 $\pi$	5 $\sigma$
Expt. [69]	19.9367	10.8742	1.3964	0.7239	0.6247	0.5144
LB $\alpha$	19.6142	10.6556	1.2549	0.7071	0.6276	0.5086
N <sub>2</sub>						
Orbital	1 $\sigma_g$	1 $\sigma_u$	2 $\sigma_g$	2 $\sigma_u$	1 $\pi_u$	3 $\sigma_g$
Expt. [70–72]	15.0492	15.0492	1.3708	0.6883	0.6233	0.5726
LB $\alpha$	14.7962	14.7950	1.2162	0.6786	0.6199	0.5682

xc potential, LB $\alpha$  [67]:

$$v_{xc,\sigma}^{\text{LB}\alpha}(\mathbf{r}, t) = \alpha v_{x,\sigma}^{\text{LSDA}}(\mathbf{r}, t) + v_{c,\sigma}^{\text{LSDA}}(\mathbf{r}, t) - \frac{\beta x_\sigma^2(\mathbf{r}, t) \rho_\sigma^{1/3}(\mathbf{r}, t)}{1 + 3\beta x_\sigma(\mathbf{r}, t) \ln\{x_\sigma(\mathbf{r}, t) + [x_\sigma^2(\mathbf{r}, t) + 1]^{1/2}\}}. \quad (18)$$

The LB $\alpha$  potential contains two parameters,  $\alpha$  and  $\beta$ , which have been adjusted in time-independent DFT calculations of several molecular systems and have the values  $\alpha = 1.19$  and  $\beta = 0.01$  [67]. The first two terms in Eq. (18),  $v_{x,\sigma}^{\text{LSDA}}$  and  $v_{c,\sigma}^{\text{LSDA}}$  are the exchange and correlation potentials within the local spin density approximation (LSDA). The last term in Eq. (18) is the gradient correction with  $x_\sigma(\mathbf{r}) = |\nabla \rho_\sigma(\mathbf{r})|/\rho_\sigma^{4/3}(\mathbf{r})$ , which ensures the proper long-range asymptotic behavior  $v_{xc,\sigma}^{\text{LB}\alpha} \rightarrow -1/r$  as  $r \rightarrow \infty$ . The potential (18) has proved to be reliable in molecular TDDFT studies [47, 68]. The correct long-range asymptotic behavior of the LB $\alpha$  potential is crucial in photoionization problems since it allows to reproduce accurate MO energies, and the proper treatment of the molecular continuum. Table II lists the MO energies calculated with the LB $\alpha$  potential, using 50 grid points in  $\xi$  and 30 grid points in  $\eta$ . The agreement of the calculated valence MO energies with the experimental data is well within 0.01 a.u.

Once the time-dependent wave functions and the time-dependent electron densities are obtained, we can calculate the time-dependent (multiphoton) ionization probability of an individual spin-orbital according to

$$P_{i,\sigma} = 1 - N_{i,\sigma}(t) \quad (19)$$

where

$$N_{i,\sigma}(t) = \langle \psi_{i,\sigma}(t) | \psi_{i,\sigma}(t) \rangle \quad (20)$$

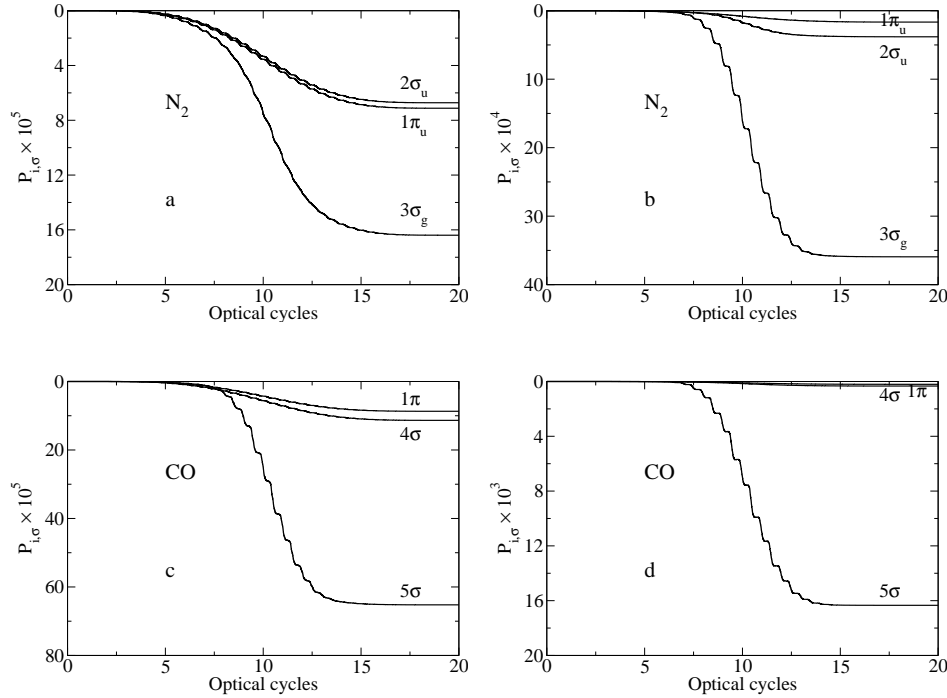


FIG. 4: The time-dependent population of electrons in different spin orbitals of CO and N<sub>2</sub> in 800 nm, sin<sup>2</sup> pulse laser field, with 20 optical cycles in pulse duration. N<sub>2</sub> molecule (a)  $5 \times 10^{13}$  W/cm<sup>2</sup>, (b)  $1 \times 10^{14}$  W/cm<sup>2</sup>, CO molecule (c)  $5 \times 10^{13}$  W/cm<sup>2</sup>, (d)  $1 \times 10^{14}$  W/cm<sup>2</sup>.

is the time-dependent population (survival probability) of the  $i\sigma$ -th spin-orbital.

Figure 4 presents the time-dependent (multiphoton) ionization probability of individual spin orbital, as defined in Eq. (19). The slope of the decay of the electron population in time determines the ionization rate. The laser (electric) field is assumed to be parallel to the internuclear axis, and the internuclear distance for the CO ( $R_e = 2.132 a_0$ ) and N<sub>2</sub> ( $R_e = 2.072 a_0$ ) molecules is fixed at its equilibrium distance  $R_e$ . Results for two laser intensities ( $5 \times 10^{13}$  W/cm<sup>2</sup> and  $1 \times 10^{14}$  W/cm<sup>2</sup>) and a wavelength of 800 nm, 20-optical-cycle laser pulse are shown for CO and N<sub>2</sub>. The orbital structure and ionization potentials of the two molecules under consideration are close to each other. That is why one can expect similar behavior in the laser field with the same wavelength and intensity. The multiphoton ionization in the laser field is dominated by HOMO, that is  $3\sigma_g$  in N<sub>2</sub> and  $5\sigma$  in CO. As one can see from Figs. 4(a) and 4(c), at lower intensity  $5 \times 10^{13}$  W/cm<sup>2</sup>, the HOMO survival probabilities of N<sub>2</sub> and CO are close to each other. However, at higher intensities, the difference becomes more pronounced, at the intensity  $1 \times 10^{14}$  W/cm<sup>2</sup>, the ionization probability of CO is much larger than that of N<sub>2</sub> (Figs. 4(b) and 4(d)). The explanation of the phenomenon can be as follows. In intense low-frequency laser fields, the multiphoton ionization occurs mainly in the tunneling regime. In this picture, the ionization takes place

TABLE III: HOMO energies of N<sub>2</sub> and CO molecules in DC electric field (positive field direction is from C to O).

Electric field (a.u.)	N <sub>2</sub> HOMO energy (a.u.)	CO HOMO energy (a.u.)
0	-0.5682	-0.5086
$0.7549 \times 10^{-2}$	-0.5681	-0.5149
$-0.7549 \times 10^{-2}$	-0.5681	-0.5026

in the DC field with slowly varying amplitude from zero to its peak value. The width of the potential barrier depends on the field strength; the stronger the field, the narrower the barrier. Thus the ionization occurs mainly at the peak values of the field strength. The probability of the tunneling ionization is very sensitive with respect to the HOMO energy. However, in the external field this energy is changed due to the Stark shift. The nitrogen molecule is symmetric with respect to inversion, that is why the Stark shift in the DC field is quadratic in the field strength and its value is quite small. On the contrary, the carbon monoxide molecule has a permanent dipole moment, and the DC Stark shift is linear in the field strength; at the peak values of the field, the HOMO energy can differ significantly from its unperturbed value. We have performed the self-consistent DFT calculations of N<sub>2</sub> and CO in the DC electric field parallel to the molecular axis to see how large the Stark shift can change the ionization potential of the molecule. On Table III we show the HOMO energies computed at the field strength  $0.7549 \times 10^{-2}$  a.u. which corresponds to the intensity  $2 \times 10^{12}$  W/cm<sup>2</sup>. As one can see, even in the field as weak as  $2 \times 10^{12}$  W/cm<sup>2</sup>, the shift of the HOMO energy in CO molecule is large. The shift depends on the direction of the external field with respect to the position of the carbon and oxygen nuclei. In one direction the energy level becomes higher, and in the other direction it becomes lower than the unperturbed level. Decrease of the binding energy will result in the enhanced ionization. In intense low-frequency laser fields, this effect can be responsible for the enhancement of ionization of CO molecule as compared with N<sub>2</sub>.

#### IV-2. High-Order Harmonic Generation of Heteronuclear and Homonuclear Diatomic Molecules in Intense Laser Fields

After the time-dependent single electron wave functions  $\{\psi_{i\sigma}\}$  are obtained, the total electron density  $\rho(\mathbf{r}, t)$  can be determined. The time-dependent induced dipole moment can now be calculated as

$$d(t) = \int d^3r \, z\rho(\mathbf{r}, t) = \sum_{i\sigma} d_{i\sigma}(t), \quad (21)$$

where

$$d_{i\sigma}(t) = n_{i\sigma} \langle \psi_{i\sigma}(\mathbf{r}, t) | z | \psi_{i\sigma}(\mathbf{r}, t) \rangle, \quad (22)$$

is the induced dipole moment of the  $i\sigma$ -th spin orbital, and  $n_{i\sigma}$  is its electron occupation number. The power spectrum of the HHG is then acquired by taking the Fourier transform of the total time-dependent induced dipole moment  $d(t)$ :

$$S(\omega) = \frac{4\omega^4}{3c^3} \left| \frac{1}{t_f - t_i} \int_{t_i}^{t_f} d(t) e^{-i\omega t} dt \right|^2. \quad (23)$$

Here  $c$  is the speed of light, and  $S(\omega)$  has the meaning of the energy emitted per unit time at the particular photon frequency  $\omega$ . In figures 5–6 we present the HHG power spectra

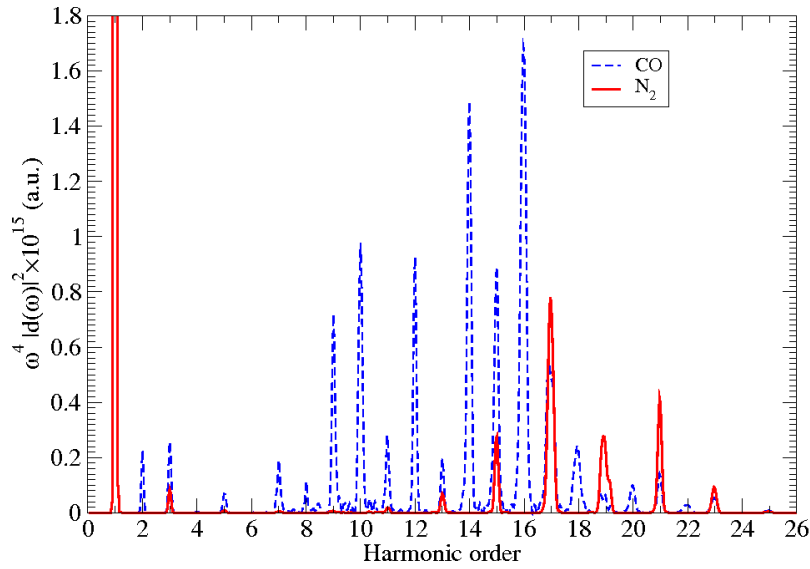


FIG. 5: Comparison of the HHG power spectra of CO and N<sub>2</sub>, in 800 nm,  $5 \times 10^{13}$  W/cm<sup>2</sup> sin<sup>2</sup> pulse laser field.

(Eq. (23)) for the laser field intensities  $5 \times 10^{13}$  W/cm<sup>2</sup>, and  $1 \times 10^{14}$  W/cm<sup>2</sup>. An important difference between the N<sub>2</sub> and CO spectra is that the latter contain even as well as odd harmonics. Generation of even harmonics is forbidden in systems with inversion symmetry, such as atoms and homonuclear diatomic molecules. This selection rule does not apply to the heteronuclear molecules with no inversion center (CO). From Figs. 5–6, one can see that in general HHG is more efficient in CO than in N<sub>2</sub>. However, for higher harmonics (17 and above) the N<sub>2</sub> spectra become dominant at the same laser intensity. As the laser intensity increases, the maximum in the power spectra is shifted towards higher harmonics.

To investigate the detailed spectral and temporal structure of HHG for homonuclear and heteronuclear systems, we perform the time-frequency analysis by means of the wavelet transform of the total induced dipole moment  $d(t)$  [46, 73],

$$d_\omega(t) = \int d(t) \sqrt{\frac{\omega}{\tau}} e^{i\omega(t-t_0)} e^{-(\omega(t-t_0))^2/2\tau^2} dt. \quad (24)$$

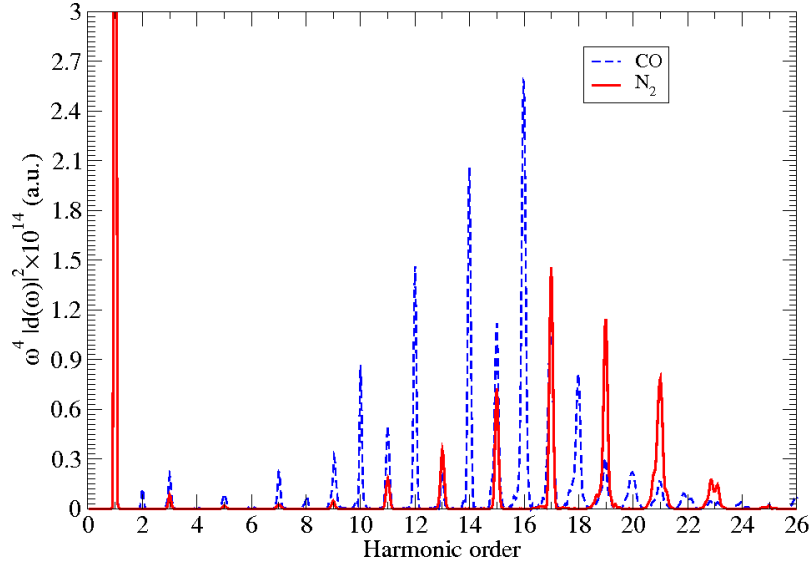


FIG. 6: Comparison of the HHG power spectra of CO and N<sub>2</sub>, in 800 nm,  $1 \times 10^{14}$  W/cm<sup>2</sup> sin<sup>2</sup> pulse laser field.

The parameter  $\tau = 15$  is chosen to perform the wavelet transformation in the following study.

The peak emission times,  $t_e$ , represent the instance when the maxima of the dipole time profile occur, and semiclassically are interpreted as the electron-ion recollision times [73]. For the case of the N<sub>2</sub> molecule, the time profiles of the 19th to 25th harmonic orders are shown in Fig. 7(a). There are two emissions occurring at each optical cycle, and the most prominent bursts take place at the center of the laser field envelope. The time profiles of the superimposed harmonics are rather uniform among themselves implicating that the harmonics are partially synchronized. More importantly for the CO molecule, a distinct feature possibly characteristic of all heteronuclear diatomic systems is observed in Fig. 7(b) for the harmonic orders 22th to 26th. The number of dominant emissions per optical cycle is now limited to only one. This finding is in contrast with results normally obtained in the HHG for atoms and homogeneous molecules in which two bursts per optical cycle are observed. The spectral profiles are as uniform as those obtained for N<sub>2</sub>, though the CO harmonics appear to be more synchronized than those of N<sub>2</sub>. In this research, we present a detailed comparison of the very high-order nonlinear optical response of the homonuclear N<sub>2</sub> and heteronuclear CO diatomic molecules in intense ultrashort laser fields by means of a TDDFT with correct asymptotic long-range ( $-1/r$ ) potential to ensure individual spin-orbital has the proper ionization potential. We consider only the case that the molecular axis is aligned with the laser beam direction. This is justified based on the recent experimental development of the laser molecular alignment techniques [74–77]. We found that although CO has only a very small permanent dipole moment, qualitatively different nonlinear optical responses are predicted for CO and N<sub>2</sub>. First, the MPI rate



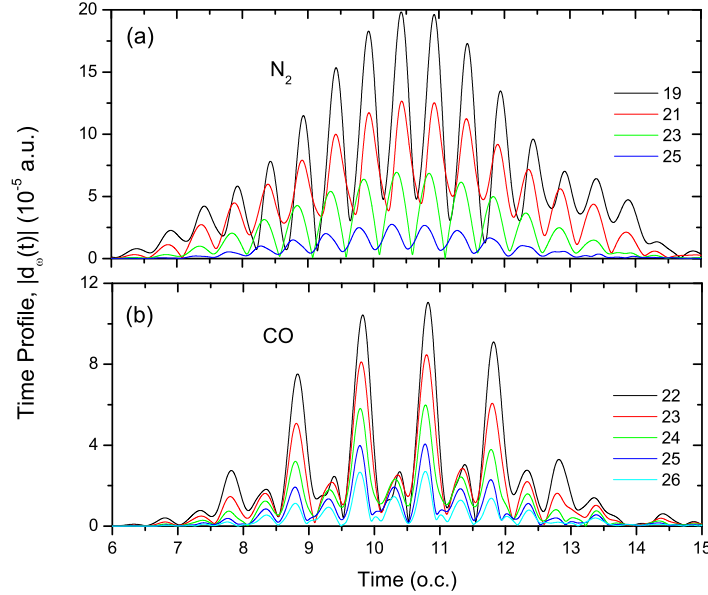


FIG. 7: Time profiles for (a)  $N_2$  and (b)  $CO$ . Laser intensity used is  $5 \times 10^{13}$  W/cm<sup>2</sup>, wavelength used is 800 nm, with 20 optical cycles in pulse duration.

for the heteronuclear diatomic  $CO$  molecules is larger than that for the  $N_2$  homonuclear diatomic molecules. Second, while the laser excitation of the  $N_2$  molecules can generate only odd harmonics, both even and odd harmonics can be produced for the  $CO$  case. In this connection, we note that the even-order harmonics were also predicted in an earlier study of the HHG of a one-dimensional model HD with unequal nuclear mass [78]. In this model, even-order harmonics can be produced only by means of the breakdown of the Born-Oppenheimer approximation. However, in our *ab initio* 3D study of  $CO$  with unequal nuclear mass and charge, even-order harmonics can still be produced when the internuclear separation is fixed. Third, from our wavelet time-frequency analysis, we found that there are two dominant rescattering (and harmonic emission) events within each optical cycle for the  $N_2$  molecules, while there is only one dominant rescattering event for the  $CO$  molecules.

### IV-3. HHG Spectra of Homonuclear and Heteronuclear Diatomic Molecules: Exploration of Multiple Orbital Contributions

In this section, we explore the nonlinear response of individual molecular orbitals (MO) to the laser field and their dynamic role in formation of the HHG spectra of multi-electron heteronuclear and homonuclear diatomic molecules [79]. We analyze the effect of asymmetry of the heteronuclear molecules on their HHG spectra, a subject of largely unexplored area of intense field molecular physics. In contrast with the homonuclear molecules which generate only odd harmonics of the laser frequency, oriented heteronuclear molecules

can produce even harmonics as well [47]. We identify the patterns of constructive and destructive interference of the orbital contributions to the total HHG spectrum. In the high-energy part of the HHG spectrum, the interference of contributions from different MO is mostly constructive for the heteronuclear molecules and destructive for the homonuclear molecules. We present an all-electron nonperturbative investigation of the HHG mechanisms taking into account the detailed electronic structure and the responses of individual electrons and using  $N_2$ ,  $F_2$ ,  $CO$ ,  $BF$ , and  $HF$  as examples ( $N_2$ ,  $CO$ , and  $BF$  are isoelectronic molecules with 14 electrons). The ground state electronic configuration of  $N_2$  and  $F_2$  (homonuclear molecules) is  $1\sigma_g^2 1\sigma_u^2 2\sigma_g^2 2\sigma_u^2 1\pi_u^4 3\sigma_g^2$  and  $1\sigma_g^2 1\sigma_u^2 2\sigma_g^2 2\sigma_u^2 3\sigma_g^2 1\pi_u^4 1\pi_g^4$ , respectively. The heteronuclear molecules  $CO$  and  $BF$  have the ground state electronic configuration of  $1\sigma^2 2\sigma^2 3\sigma^2 4\sigma^2 1\pi^4 5\sigma^2$  and for the  $HF$  molecule its ground state configuration appears as  $1\sigma^2 2\sigma^2 3\sigma^2 1\pi^4$ . Table IV lists the MO energies calculated with the  $LB\alpha$  potential, using 50 grid points in  $\xi$  and 30 grid points in  $\eta$ . The agreement of the calculated valence MO energies with the experimental data is well within 0.01 a.u.

For the  $CO$  molecule, the HOMO ( $5\sigma$ ) is dominant for the whole HHG spectrum (Fig. 8); other orbitals contribute much less. The distinct harmonic peaks are seen up to the order 30. In  $CO$ , the  $5\sigma$  (HOMO) permanent dipole is 1.57 a.u. which is much larger than that of the other orbitals. The density for the  $5\sigma$  (and  $2\sigma$ ) is mostly localized on the carbon atom. For all other orbitals the density is localized on the oxygen atom. Looking at the time-dependent orbital dipoles for the  $CO$  molecule (Fig. 9), we can see that all other orbitals that are localized on the oxygen atom are in phase and  $5\sigma$  (carbon) is out of phase in time.

The  $N_2$  molecule has dipole amplitudes that follow the trend:

$$d_{2\sigma_g} < d_{1\pi_u} < d_{total} < d_{3\sigma_g} < d_{2\sigma_u}. \quad (25)$$

The orbital dipole moments  $2\sigma_g$ ,  $1\pi_u$ , and  $2\sigma_u$  are oscillating with the same sign (in phase) of the total dipole, the  $3\sigma_g$  has opposite sign (out of phase). So when we look at the two orbital dipole amplitudes  $2\sigma_u$  and  $3\sigma_g$  with similar intensities, they oscillate in time with different sign, canceling each other out (Fig. 10), leading to a smaller total dipole.

The behavior of the HHG spectrum (Fig. 11) for  $N_2$  is quite different than that of a heteronuclear diatomic molecule. The HOMO ( $3\sigma_g$ ) is dominant in the middle part of the spectrum (again up to the order 31). However, starting the 33th harmonic, the  $2\sigma_u$  orbital has a comparable contribution which interferes destructively with that of  $3\sigma_g$ . Thus the result of interference is much lower than both of the single orbital spectra. Then this two-orbital spectrum becomes comparable in magnitude with the  $2\sigma_g$ -only HHG. Again, the destructive contributions takes place, and the result is much lower than any of the single orbital contributions. In summary, we can say that the long HHG spectrum of  $N_2$  is a collective multielectron effect. Destructive interference between  $2\sigma_u$  and  $3\sigma_g$  orbital contributions makes the resulting total HHG spectrum lower in amplitude with distinct harmonic peaks up to the order 49. Note that single orbital HHG do not have distinct peaks, just a smooth background, so the peaks in the high harmonic part of the total HHG spectra are the pure multielectron interference effect.

In contrast to the  $N_2$  molecule, the full destructive interference is not possible in  $CO$

TABLE IV: Comparison of the field-free molecular orbital energy levels of  $F_2$ ,  $BF$ ,  $CO$ ,  $N_2$  and  $HF$ , calculated with the  $LB\alpha$  potential, and the experimental ionization potentials (in a.u.).

$F_2$							
Orbital	$1\sigma_g$	$1\sigma_u$	$2\sigma_g$	$2\sigma_u$	$3\sigma_g$	$1\pi_u$	$1\pi_g$
Expt. [80]	25.601	25.609	1.5342	1.377	0.775	0.691	0.5832
$LB\alpha$	25.1531	25.1531	1.4508	1.2252	0.7907	0.6939	0.5739
$BF$							
Orbital	$1\sigma$	$2\sigma$	$3\sigma$	$4\sigma$	$1\pi$	$5\sigma$	
Expt. [81, 82]						0.4085	
$LB\alpha$	25.1669	7.1745	1.4140	0.7763	0.6970	0.3895	
$CO$							
Orbital	$1\sigma$	$2\sigma$	$3\sigma$	$4\sigma$	$1\pi$	$5\sigma$	
Expt. [69]	19.9367	10.8742	1.3964	0.7239	0.6247	0.5144	
$LB\alpha$	19.6142	10.6556	1.2549	0.7071	0.6276	0.5086	
$N_2$							
Orbital	$1\sigma_g$	$1\sigma_u$	$2\sigma_g$	$2\sigma_u$	$1\pi_u$	$3\sigma_g$	
Expt. [83–85]	15.0492	15.0492	1.3708	0.6883	0.6233	0.5726	
$LB\alpha$	14.7962	14.7950	1.2162	0.6786	0.6199	0.5682	
$HF$							
Orbital	$1\sigma$	$2\sigma$	$3\sigma$	$1\pi$			
Expt. [86]	25.5132	1.4545	0.7284	0.5898			
$LB\alpha$	25.0786	1.3074	0.7070	0.5741			

because of the broken g-u symmetry. The induced dipole moment of the HOMO  $5\sigma$  is so large that no other orbital can make a comparable contribution. To prove this point about heteronuclear and homonuclear diatomic molecules, we look at  $F_2$ ,  $BF$ , and the heteronuclear molecule that has the greatest dipole moment,  $HF$ . Here, we can see if these molecules exhibit similar properties of  $CO$  and  $N_2$ . We see the same characteristics in  $F_2$ , as we can see in  $N_2$ . The orbital dipole moments of  $2\sigma_u$  and  $1\pi_g$  are oscillating out of phase, from other orbitals, including the total. So when we look at the two orbital dipole amplitudes  $1\pi_u$  and  $1\pi_g$ , they oscillate in time with different sign, canceling each other out (Fig. 12), leading to a smaller total dipole. The behavior of the HHG spectrum of  $F_2$  is similar to that of  $N_2$ . If we look at Fig. 13, the  $1\pi_u$  and  $1\pi_g$  orbitals dominate the HHG spectrum, and it has much greater intensity than that of the total HHG. In this Fig. 13, we see there is destructive interference between the contributions from the  $1\pi_u$  and  $1\pi_g$

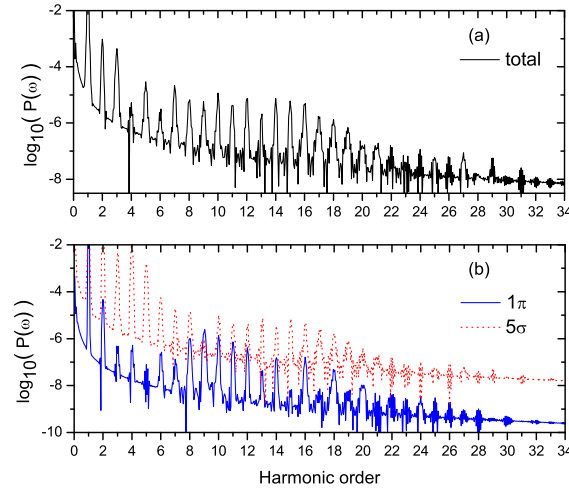


FIG. 8: Total (a) and orbital (b) harmonic power spectra of the CO molecule in the  $\sin^2$  laser pulse with a peak intensity of  $I_0 = 1 \times 10^{14}$  W/cm<sup>2</sup>. The laser pulse has a wavelength of 800 nm and a time duration of 20 optical cycles.

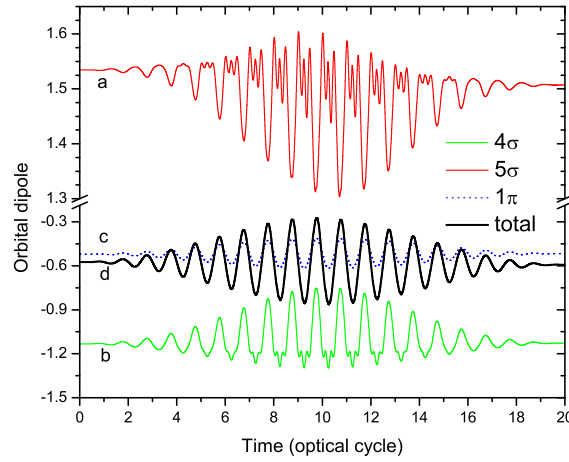


FIG. 9: Time-dependent orbital (a,  $5\sigma$ ; b,  $4\sigma$ ; c,  $1\pi$ ) and total (d) dipole moments of the CO molecule in the  $\sin^2$  laser pulse with a peak intensity of  $I_0 = 1 \times 10^{14}$  W/cm<sup>2</sup>. The laser pulse has a wavelength of 800 nm and a time duration of 20 optical cycles. All dipoles are in a.u.

orbitals, we explained this previously with their dipole moments being out of phase with one another. Since these two orbitals ( $1\pi_u$  and  $1\pi_g$ ) have the greatest amplitude of the induced dipole, they will have the greatest contributions to the power spectrum.

Previously, we only looked at the CO molecule for the heteronuclear diatomic system,

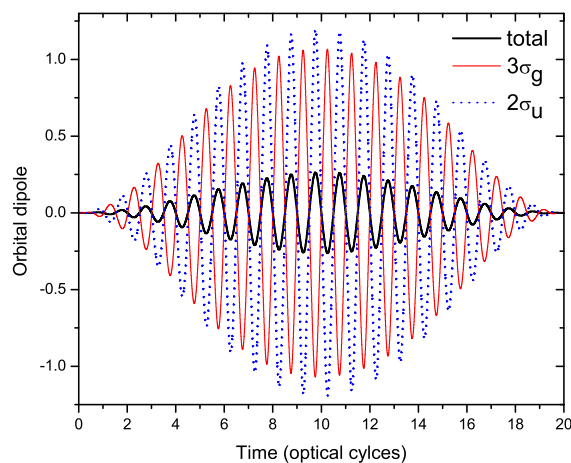


FIG. 10: Time-dependent orbital and total dipole moments of the  $N_2$  molecule in the  $\sin^2$  laser pulse with a peak intensity of  $I_0 = 1 \times 10^{14}$  W/cm<sup>2</sup>. The laser pulse has a wavelength of 800 nm and a time duration of 20 optical cycles. All dipoles are in a.u.

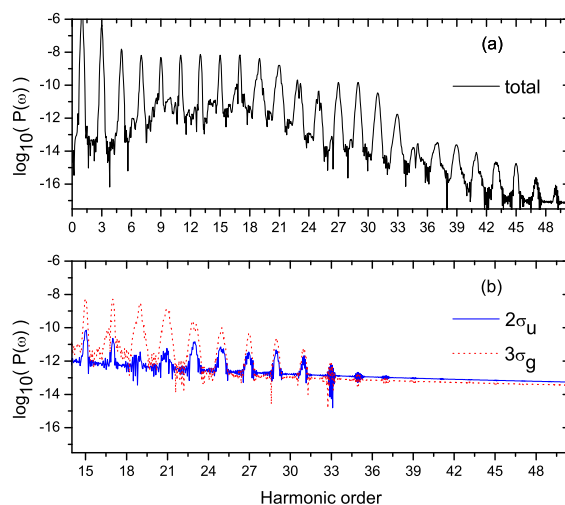


FIG. 11: Total and orbital harmonic power spectra of the  $N_2$  molecule in the  $\sin^2$  laser pulse with a peak intensity of  $I_0 = 1 \times 10^{14}$  W/cm<sup>2</sup>. The laser pulse has a wavelength of 800 nm and a time duration of 20 optical cycles.

and saw where the HOMO dominates the HHG spectrum and dipole moment. Now we examine two other heteronuclear molecules (BF and HF), and see if their characteristics resemble that of the CO molecule. To understand the HHG spectrum, again we look at the orbital dipole moment of BF. Fig. 14 shows that the  $5\sigma$  orbital (like that of CO, since they

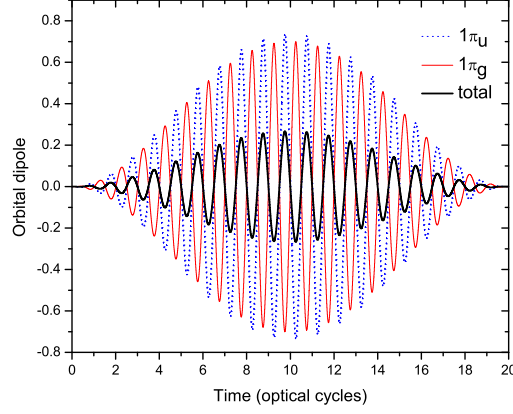


FIG. 12: Time-dependent orbital and total dipole moments of the  $F_2$  molecule in the  $\sin^2$  laser pulse with a peak intensity of  $I_0 = 1 \times 10^{14} \text{ W/cm}^2$ . The laser pulse has a wavelength of 800 nm and a time duration of 20 optical cycles. All dipoles are in a.u.

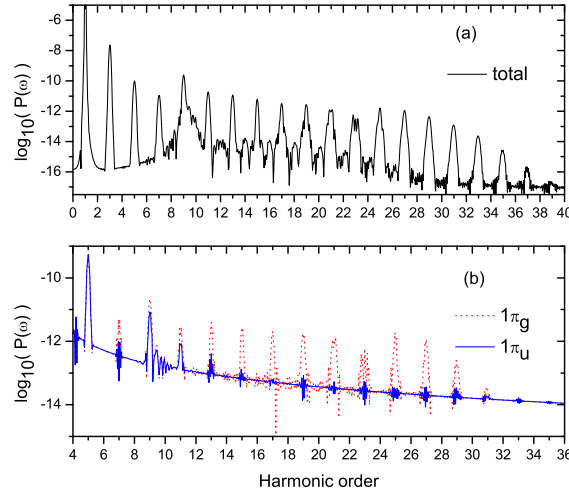


FIG. 13: Total (a) and orbital (b) harmonic power spectra of the  $F_2$  molecule in the  $\sin^2$  laser pulse with a peak intensity of  $I_0 = 1 \times 10^{14} \text{ W/cm}^2$ . The laser pulse has a wavelength of 800 nm and a time duration of 20 optical cycles.

are isoelectronic) has the greatest dipole moment. This is understandable, since most of the electronic density resides on the fluorine atom. The fluorine atom is more electronegative than that of the boron atom, so it will have the greater electron density. As previous seen in the CO molecule, BF has the same physical characteristics of its orbital HHG spectrum. Fig. 15 shows that HOMO ( $5\sigma$ ) has the greatest contribution to the total HHG.

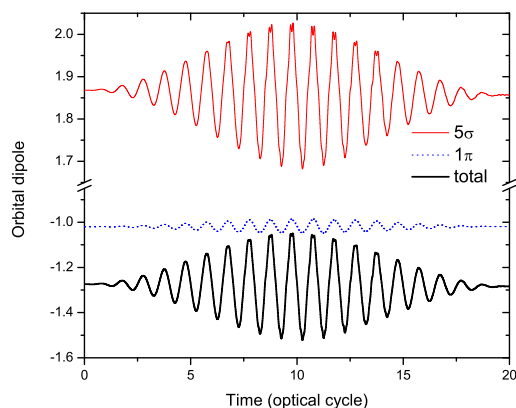


FIG. 14: Time-dependent orbital and total dipole moments of the BF molecule in the  $\sin^2$  laser pulse with a peak intensity of  $I_0 = 1 \times 10^{14}$  W/cm<sup>2</sup>. The laser pulse has a wavelength of 800 nm and a time duration of 20 optical cycles. All dipoles are in a.u.

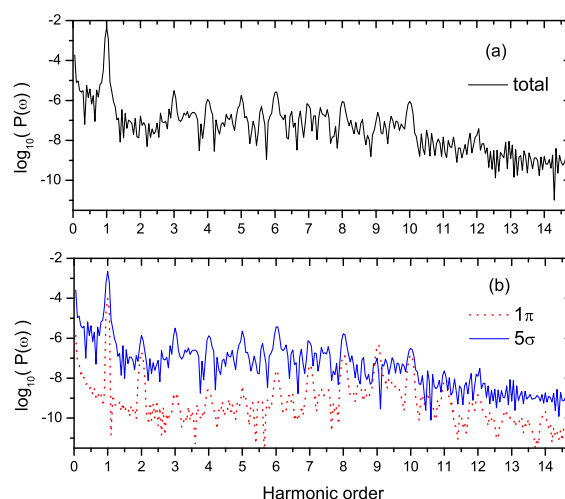


FIG. 15: Total (a) and orbital (b) harmonic power spectra of the BF molecule in the  $\sin^2$  laser pulse with a peak intensity of  $I_0 = 1 \times 10^{14}$  W/cm<sup>2</sup>. The laser pulse has a wavelength of 800 nm and a time duration of 20 optical cycles.

Now we will study the heteronuclear molecule that has the greatest permanent dipole moment, and look at the physical characteristics of hydrogen fluoride. HF has a permanent dipole moment of 1.820 Debye, where most of the electron density resides on the fluorine atom. For HF molecule, the HOMO is the  $1\pi$  orbital, and it has the greatest negative value of the orbital dipole moment (see Fig. 16). However, when we look at the orbital

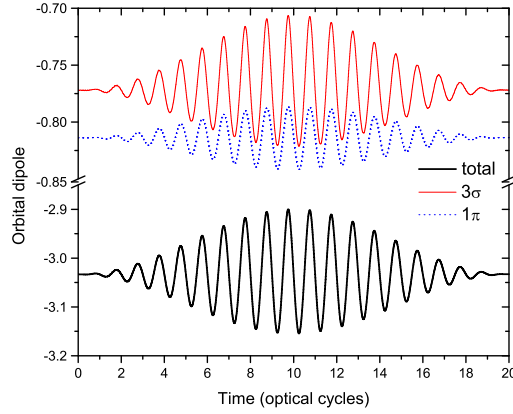


FIG. 16: Time-dependent orbital and total dipole moments of the HF molecule in the  $\sin^2$  laser pulse with a peak intensity of  $I_0 = 1 \times 10^{14}$  W/cm<sup>2</sup>. The laser pulse has a wavelength of 800 nm and a time duration of 20 optical cycles. All dipoles are in a.u.

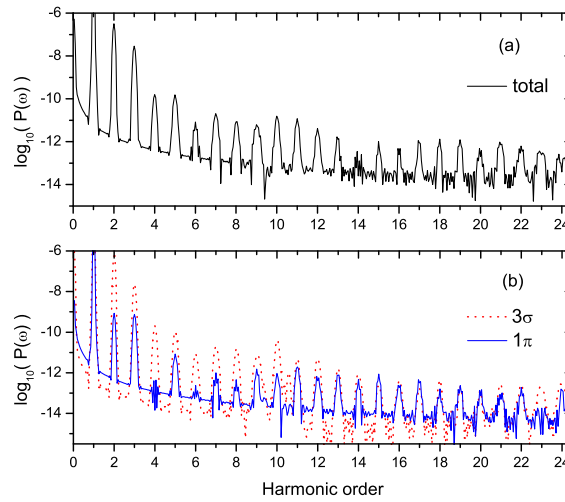


FIG. 17: Total (a) and orbital (b) harmonic power spectra of the HF molecule in the  $\sin^2$  laser pulse with a peak intensity of  $I_0 = 1 \times 10^{14}$  W/cm<sup>2</sup>. The laser pulse has a wavelength of 800 nm and a time duration of 20 optical cycles.

HHG spectrum (Fig. 17), we see the greatest orbital contribution to the HHG spectrum was from  $3\sigma$ , not the HOMO orbital ( $1\pi$ ). Since the field is linearly polarized to the  $z$  axis and the  $1\pi$  orbital is perpendicular to the  $z$  axis, the induced dipole moment is aligned not with the  $1\pi$  orbital but with the  $3\sigma$  orbital. We see between harmonic order peaks (even and odd), the  $1\pi$  orbital has greater intensity than that of the  $3\sigma$  orbital. At peak values



(even and odd harmonic orders) the  $3\pi$  orbital has almost the same intensity as that of the total HHG spectrum. We conclude that HF follows the same orbital characteristics of other heteronuclear molecules studied (CO and BF).

Our analysis of the HHG spectra for the parallel orientation of the molecular axis with respect to the polarization of the laser field reveals that homonuclear molecules have destructive interference between the orbital contributions to the total harmonic signal. This happens because the induced dipole moments of different orbitals oscillate in time with opposite phases, so their contributions are canceled out in the total dipole moment. Therefore a close look at the induced dipole moment of the homonuclear diatomic molecules can give predictions of what orbital contributions will interfere destructively in the total HHG spectrum. The destructive interference in the HHG spectrum accounts for the unexpected observation that some of the individual orbitals harmonic power spectra have greater intensity than that of the total HHG. The HHG process by the heteronuclear diatomic molecules has a quite different characteristic. First, heteronuclear molecules can generate even and odd harmonics since they lack the inversion symmetry. Second, for all the studied heteronuclear molecules, the HOMO contribution to the total HHG spectrum is by far dominant, and the total harmonic signal has almost the same intensity as that produced by HOMO only. The interference between the different orbitals in the total HHG spectrum is mostly constructive. The same features are observed in the time-dependent induced dipole moments, with the HOMO dipole moment having the largest oscillation magnitude.

## V. ORIENTATION-DEPENDENT MULTIPHOTON IONIZATION AND HIGH-ORDER HARMONIC GENERATION OF DIATOMIC MOLECULES

### V-1. AN ALL-ELECTRON TDDFT APPROACH FOR $N_2$ AND $F_2$ MOLECULES

In our calculations of multiphoton processes in  $N_2$  and  $F_2$  [56, 87], we used the laser wavelength 800 nm ( $\omega_0 = 0.056954$  a.u.) and the sine-squared envelope with 20 optical cycles. The propagation procedure based on Eq. (13) is applied sequentially starting at  $t = 0$  and ending at  $t = T$ . As a result, the spin orbitals  $\psi_{n\sigma}(\xi, \eta, \varphi, t)$  are obtained on a uniform time grid within the interval  $[0, T]$ . The space domain is finite with the linear dimension restricted by the end point  $R_b$ . We choose  $R_b = 40$  a.u.; the corresponding space volume contains all relevant physics for the laser field parameters used in the calculations. Between 20 a.u. and 40 a.u. we apply an absorber which smoothly brings down the wave function for each spin orbital without spurious reflections. Absorbed parts of the wave packet localized beyond 20 a.u. describe unbound states populated during the ionization process. Because of the absorber, the normalization integrals of the wave functions  $\psi_{n\sigma}(\mathbf{r}, t)$  decrease in time. Calculated after the pulse, they give the survival probabilities  $\mathcal{P}_{n\sigma}^{(s)}$  for each spin orbital:

$$\mathcal{P}_{n\sigma}^{(s)} = \int d^3r |\psi_{n\sigma}(\mathbf{r}, T)|^2. \quad (26)$$

TABLE V: Absolute values of spin orbital energies of N<sub>2</sub>, F<sub>2</sub>, and Ar. (A) DFT calculations [56] (eV). (B) Experimental ionization energies (eV).

Molecule	Spin-orbital	A	B	
N <sub>2</sub>	2 $\sigma_u$	18.5	18.7	(Ref. [88])
	1 $\pi_u$	16.9	17.2	(Ref. [88])
	3 $\sigma_g$ (HOMO)	15.5	15.6	(Ref. [88])
F <sub>2</sub>	3 $\sigma_g$	21.9	21.0	(Ref. [89])
	1 $\pi_u$	19.2	19.0	(Ref. [89])
	1 $\pi_g$ (HOMO)	16.0	15.7	(Ref. [89])
Ar	3s	29.0	29.3	(Ref. [90])
	3p	15.3	15.8	(Ref. [90])

Then one can define the spin orbital ionization probabilities  $\mathcal{P}_{n\sigma}^{(i)}$  as

$$\mathcal{P}_{n\sigma}^{(i)} = 1 - \mathcal{P}_{n\sigma}^{(s)}. \quad (27)$$

We note that the quantities  $\mathcal{P}_{n\sigma}^{(s)}$  represent the survival probabilities for the electron occupying the unperturbed  $\psi_{n\sigma}(\mathbf{r}, t = 0)$  spin orbital *before* the laser pulse. Accordingly, the quantity  $\mathcal{P}_{n\sigma}^{(i)}$  represents the ionization probability for the electron originally occupying the unperturbed  $\psi_{n\sigma}(\mathbf{r}, t = 0)$  spin orbital.

The total survival probability  $\mathcal{P}^{(s)}$  can be calculated as a product of the spin orbital survival probabilities:

$$\mathcal{P}^{(s)} = \prod_{n\sigma} \mathcal{P}_{n\sigma}^{(s)} = \prod_{n\sigma} \left(1 - \mathcal{P}_{n\sigma}^{(i)}\right), \quad (28)$$

and the total ionization probability can be written as

$$\mathcal{P}^{(i)} = 1 - \mathcal{P}^{(s)} = 1 - \prod_{n\sigma} \left(1 - \mathcal{P}_{n\sigma}^{(i)}\right). \quad (29)$$

The total ionization probability as defined by Eq. (29) reduces to the sum of the spin orbital probabilities only in the limit of the weak laser field (small  $\mathcal{P}_{n\sigma}^{(i)}$ ). In the calculations, we used the experimental values of the equilibrium internuclear separations for the diatomic molecules [63] (2.074 a.u. for N<sub>2</sub> and 2.668 a.u. for F<sub>2</sub>). In Table V, we summarize the energies for the spin orbitals that have a significant contribution to MPI and HHG and the

corresponding experimental vertical ionization energies. Also presented are the data for the companion Ar atom which has an ionization potential close to that of  $\text{N}_2$  and  $\text{F}_2$  and is expected to manifest close ionization probabilities as well. The agreement between the calculated and experimental values is fairly good for all three systems indicating a good quality of the  $\text{LB}\alpha$  exchange-correlation potential.

### V-1-1. Multiphoton ionization

We present the orientation-dependent MPI probabilities for  $\text{N}_2$  molecule at the peak intensity  $2 \times 10^{14} \text{ W/cm}^2$  (Fig. 18). The orientation dependence of the total MPI probability is in a good accord with the experimental observations [91, 92] for this molecule and reflects the symmetry of its HOMO: the maximum corresponds to the parallel orientation.

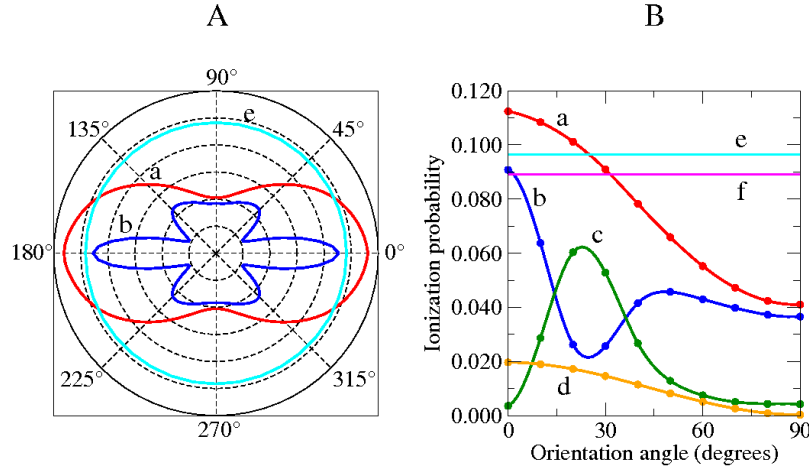


FIG. 18: MPI probabilities of  $\text{N}_2$  molecule and Ar atom for the peak intensity  $2 \times 10^{14} \text{ W/cm}^2$  in polar (panel A) and Cartesian (panel B) coordinates: (a) total probability for  $\text{N}_2$ , (b)  $3\sigma_g$  (HOMO) probability for  $\text{N}_2$ , (c)  $1\pi_u$  (HOMO-1) probability for  $\text{N}_2$ , (d)  $2\sigma_u$  probability for  $\text{N}_2$ , (e) total probability for Ar, (f)  $3p_0$  probability for Ar.

However, multielectron effects are quite important for  $\text{N}_2$ , particularly at intermediate orientation angles. In the angle range around  $30^\circ$ , the orbital probability of HOMO-1 ( $1\pi_u$ ) is larger than that of HOMO ( $3\sigma_g$ ). Despite the orbital probabilities have local minima and maxima, the total probability shows monotonous dependence on the orientation angle. With increasing the peak intensity of the laser field, the orientation angle distribution of the total ionization probability becomes more isotropic. For comparison, we show also the ionization probability of the Ar atom. As one can see from Fig. 18, the absolute values of the ionization probabilities of  $\text{N}_2$  and Ar are close to each other. However, the inner shell contributions are less important for Ar: the total probability is dominated by the highest-occupied ( $3p$ ) shell contribution. An analysis of the spin orbital energies (Table V) can help to understand the relative importance of MPI from the inner shells in  $\text{N}_2$  compared to that in Ar. The smaller the ionization potential of the electronic shell, the easier

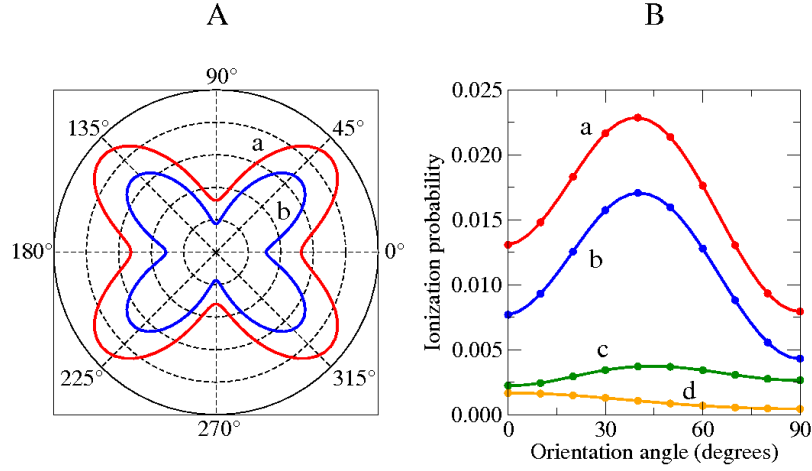


FIG. 19: MPI probabilities of F<sub>2</sub> molecule for the peak intensity  $2 \times 10^{14}$  W/cm<sup>2</sup> in polar (panel A) and Cartesian (panel B) coordinates: (a) total probability, (b)  $1\pi_g$  (HOMO) probability, (c)  $1\pi_u$  (HOMO–1) probability, (d)  $3\sigma_g$  probability.

it can be ionized. That is why HOMO is generally expected to give the main contribution to the MPI probability. However, in N<sub>2</sub> the ionization potential of HOMO–1 is quite close to that of HOMO (the difference between the calculated values is 1.4 eV), and in the strong enough laser field both shells show comparable ionization probabilities (a possible resonance between HOMO and HOMO–1 in the 800 nm laser field also favors that; see discussion of HHG in Sec.V-1-2 below). At the same time, the gap between the  $3p$  and  $3s$  spin orbital energies in Ar is much larger (our calculation gives the value 13.7 eV), and the  $3p$  contribution to the MPI probability remains dominant for all three laser intensities.

For F<sub>2</sub>, the total ionization probability appears smaller than that of N<sub>2</sub> (and Ar) at the same laser intensity  $2 \times 10^{14}$  W/cm<sup>2</sup> (Fig. 19). The ratio of the MPI probabilities of Ar and F<sub>2</sub> (at 40°) is approximately equal to 4.2. The pattern for the orientation dependence of MPI in F<sub>2</sub> resembles that experimentally observed in O<sub>2</sub> [91] since both molecules have the HOMO of the same symmetry ( $1\pi_g$ ), and the HOMO contribution is dominant at this intensity. The maximum in the orientation angle distribution of the total MPI probability points at 40°. The HOMO–1 contribution is less important than that in N<sub>2</sub>, and this is well explained by the larger gap between the HOMO and HOMO–1 energies (3.2 eV).

### V-1-2. High-order harmonic generation

For non-monochromatic fields, the spectral density of the radiation energy emitted for all the time is given by the following expression [93]:

$$S(\omega) = \frac{2\omega^4}{3\pi c^3} |\tilde{\mathbf{D}}(\omega)|^2. \quad (30)$$

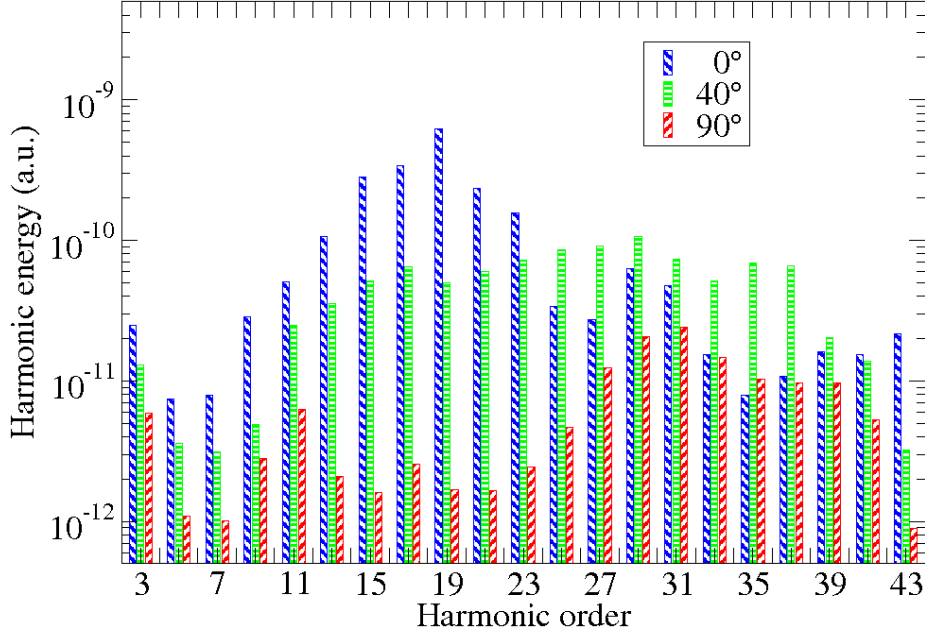


FIG. 20: Energy emitted in harmonic radiation by  $N_2$  molecule for the peak intensity  $2 \times 10^{14} \text{ W/cm}^2$ : left (blue) bar, orientation angle  $\gamma = 0^\circ$ ; middle (green) bar, orientation angle  $\gamma = 40^\circ$ ; right (red) bar, orientation angle  $\gamma = 90^\circ$ .

Here  $\omega$  is the frequency of radiation,  $c$  is the velocity of light, and  $\tilde{\mathbf{D}}(\omega)$  is a Fourier transform of the time-dependent dipole moment:

$$\tilde{\mathbf{D}}(\omega) = \int_{-\infty}^{\infty} dt \mathbf{D}(t) \exp(i\omega t). \quad (31)$$

The dipole moment is evaluated as an expectation value of the electron radius-vector with the time-dependent total electron density  $\rho(\mathbf{r}, t)$ :

$$\mathbf{D}(t) = \int d^3r \mathbf{r} \rho(\mathbf{r}, t). \quad (32)$$

The total energy  $\mathcal{E}$  emitted in the harmonic radiation can be calculated by integration of  $S(\omega)$ :

$$\mathcal{E} = \int_0^{\infty} d\omega S(\omega). \quad (33)$$

For a long enough laser pulse, the radiation energy spectrum (30) contains peaks corresponding to odd harmonics of the carrier frequency  $\omega_0$ . We define the energy  $\mathcal{E}(N_h)$  emitted in the  $N_h$ th harmonic ( $N_h$  is an odd integer number) as follows:

$$\mathcal{E}(N_h) = \int_{(N_h-1)\omega_0}^{(N_h+1)\omega_0} d\omega S(\omega). \quad (34)$$

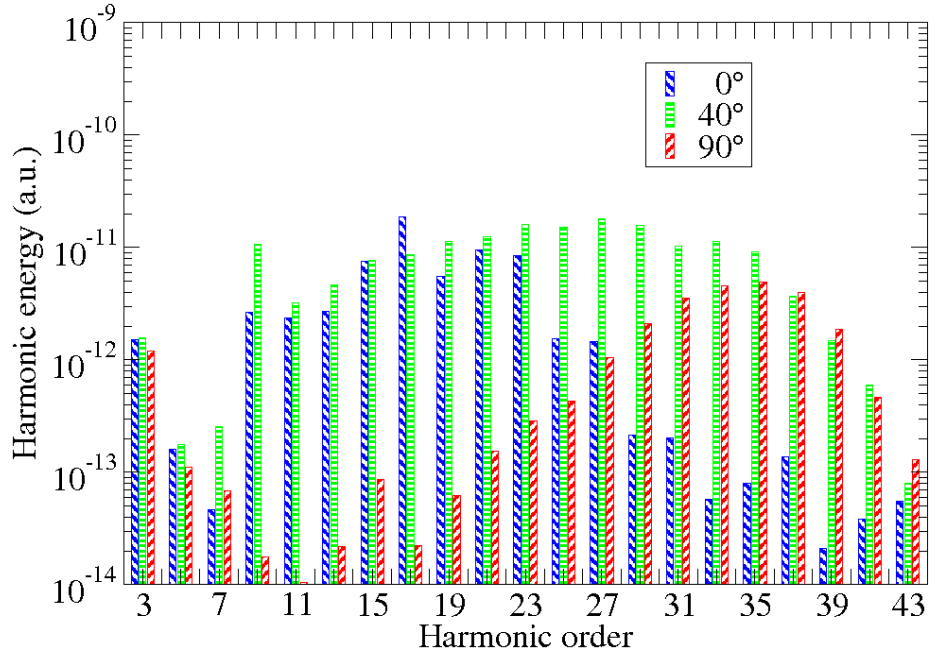


FIG. 21: Energy emitted in harmonic radiation by  $F_2$  molecule for the peak intensity  $2 \times 10^{14} \text{ W/cm}^2$ : left (blue) bar, orientation angle  $\gamma = 0^\circ$ ; middle (green) bar, orientation angle  $\gamma = 40^\circ$ ; right (red) bar, orientation angle  $\gamma = 90^\circ$ .

In Figs. 20 and 21 we present the HHG data for  $N_2$  and  $F_2$  molecules, respectively, at the peak intensity  $2 \times 10^{14} \text{ W/cm}^2$ . The cutoff position in the HHG spectrum for this intensity is expected at the harmonic order 35, in fair agreement with the computed data. To show the orientation dependence of the HHG spectra, we choose three values of the orientation angle  $\gamma$ :  $0^\circ$ ,  $40^\circ$ , and  $90^\circ$  which represent the limiting cases of the parallel and perpendicular orientation as well as the intermediate angle case. For all three orientations, the HHG signal from  $N_2$  is about an order of magnitude stronger than that from  $F_2$ ; this observation is consistent with the MPI results of Sec.V-1-1: at this intensity, the MPI signal from  $F_2$  is 4 to 10 times weaker than that from  $N_2$ , depending on the orientation. The orientation dependence of HHG also resembles that of MPI: HHG is more intense for the orientations where MPI reaches its maximum. It is clearly seen for  $F_2$  where the radiation energy at  $40^\circ$  exceeds that at other orientations for almost every harmonic. For  $N_2$ , the HHG signal at  $0^\circ$  is dominant in the low-order part of the spectrum whereas in the central part a stronger signal is observed at  $40^\circ$ . One can also see that the emission of the harmonic radiation at the perpendicular orientation ( $\gamma = 90^\circ$ ) is suppressed for both  $N_2$  and  $F_2$  in the low-order and central parts of the HHG spectra. The maximum in the harmonic energy distribution at  $90^\circ$  is shifted to higher orders. This result is in a good accord with the recent experimental measurements on  $N_2$  [94]. Also, we would like to comment on the minimum seen in the HHG spectrum of  $N_2$  (Fig. 20) at the parallel orientation near the

25th harmonic order (photon energy  $\sim 39$  eV). This minimum has been observed in the same photon energy region in a recent experimental work [95]; it appears independent of intensity and wavelength of the laser field. We take an in depth look at the multielectron effect on the HHG minimum for aligned CO molecules in the next section.

## V-2. High-Order Harmonic Generation of Aligned CO Molecules

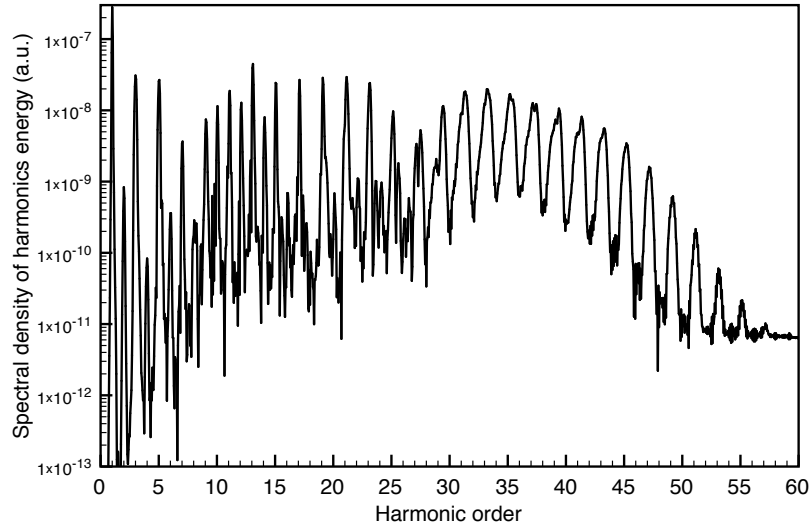


FIG. 22: Total harmonic power spectra of the CO molecule in the  $\sin^2$  laser pulse with a peak intensity of  $I_0 = 3 \times 10^{14}$  W/cm<sup>2</sup>. The laser pulse has a wavelength of 800 nm and a time duration of 20 optical cycles: orientation angle  $\gamma = 90^\circ$ .

In this section, we study the effects of correlated multielectron responses on HHG of aligned CO molecules in intense 800 nm laser pulses. Considering aligned rather than oriented heteronuclear molecules has a closer relation to the experimental situation where the aligning field creates equal numbers of molecules with opposite orientations. The average permanent dipole moment of a macroscopic sample of aligned molecules vanishes, and only odd harmonics can be generated, in contrast to oriented heteronuclear molecules where generation of even harmonics is possible. On the microscopic level, the HHG spectrum of a sample of aligned molecules can be modeled as a coherent average of the signals from two oriented molecules with opposite orientations. We have found that the high-energy part of the HHG spectrum of aligned CO molecules exhibits a strong dependence on the alignment angle between the molecular axis and the polarization direction of the laser field with the sharp minimum at the perpendicular alignment. An analysis of the HHG spectra at the perpendicular alignment revealed also two minima, one of them corresponding to the photon energy in the range 37 eV to 45 eV, and another one in the range 63 eV to 69 eV. Positions of both minima only slightly depend on the peak intensity of the laser field.

We have computed the alignment-dependent HHG spectra for CO at a range of peak intensities,  $3 \times 10^{14}$  W/cm<sup>2</sup> to  $5 \times 10^{14}$  W/cm<sup>2</sup>. (Figs. 22–25). For the laser intensity of  $3 \times 10^{14}$  W/cm<sup>2</sup>, one can see a minimum at the 27th harmonic order (Fig. 22). For higher laser intensities and the same alignment angle  $90^\circ$ , the minimum is still present but shifted to higher harmonic orders (photon energies). To explore the nature of this minimum, we analyze the individual orbital HHG spectra and their contributions to the total HHG spectrum. In Fig. 23, one can see that the  $5\sigma$ ,  $1\pi$  and  $4\sigma$  orbital spectra all have minima at the 27th harmonic. This observation suggests that the minimum has a kinematic nature, such as related to the two-center interference, and does not depend on the specific electronic structure. On the other hand, multielectron structure effects are clearly seen in the other part of the HHG spectrum, in the vicinity of the 11th harmonic where the orbital contributions are enhanced due to the resonance between the  $4\sigma$  and  $1\pi$  orbitals. However, since these orbitals are occupied, no real transitions can occur between them, that is why these two orbital contributions interfere destructively, and the total HHG spectrum does not exhibit the resonance enhancement. One can also see from Fig. 23 that the multielectron effects are very important in the central and high-energy parts of the HHG spectrum where the  $1\pi$  orbital makes comparable and even greater contribution than that of the  $5\sigma$  orbital (HOMO). In our previous work, we showed that the multielectron effects are responsible for enhanced HHG at some orientations of the molecular axis. Even strongly bound electrons may have a significant influence on the HHG process [56, 79].

At the laser intensity of  $4 \times 10^{14}$  W/cm<sup>2</sup>, the minimum in the HHG spectrum is blue shifted to the 29th harmonic order (Fig. 24). We note that in another theoretical work [96] where only the HOMO contribution to the HHG spectrum of the CO molecule was considered, the minimum at the laser intensity of  $4 \times 10^{14}$  W/cm<sup>2</sup> was detected in the vicinity of the harmonic order 50. In Fig. 25, we show alignment angle dependence of the minimum and cutoff region in the HHG spectrum at the higher laser intensity of  $5 \times 10^{14}$  W/cm<sup>2</sup>. Besides the minimum at the 29th harmonic ( $\sim 45$  eV), we can also see another minimum at the 44th order (69 eV) which is more distinct at the alignment angle  $90^\circ$  and becomes less pronounced at other angles ( $80^\circ$  and  $85^\circ$ , respectively). Also, the cutoff region of the spectrum exhibits a sharp dependence on the alignment angle, decreasing more rapidly at  $90^\circ$ .

Finally, we would like to comment on the shift of the minimum in the HHG spectrum as a function of the laser intensity. As one can see in Figs. (22–25), the minimum is shifted to higher harmonic orders as the laser intensity increases. This phenomenon was also recently discovered for CO<sub>2</sub> molecules [97]. This shift is due to the time interval between ionization and recombination steps of the HHG process. Therefore, this shift should depend linearly on the laser intensity.

## VI. CONCLUSION

In this paper, we have presented *self-interaction-free* TDDFT approaches recently developed for accurate and efficient treatment of the high-order multiphoton dynamics



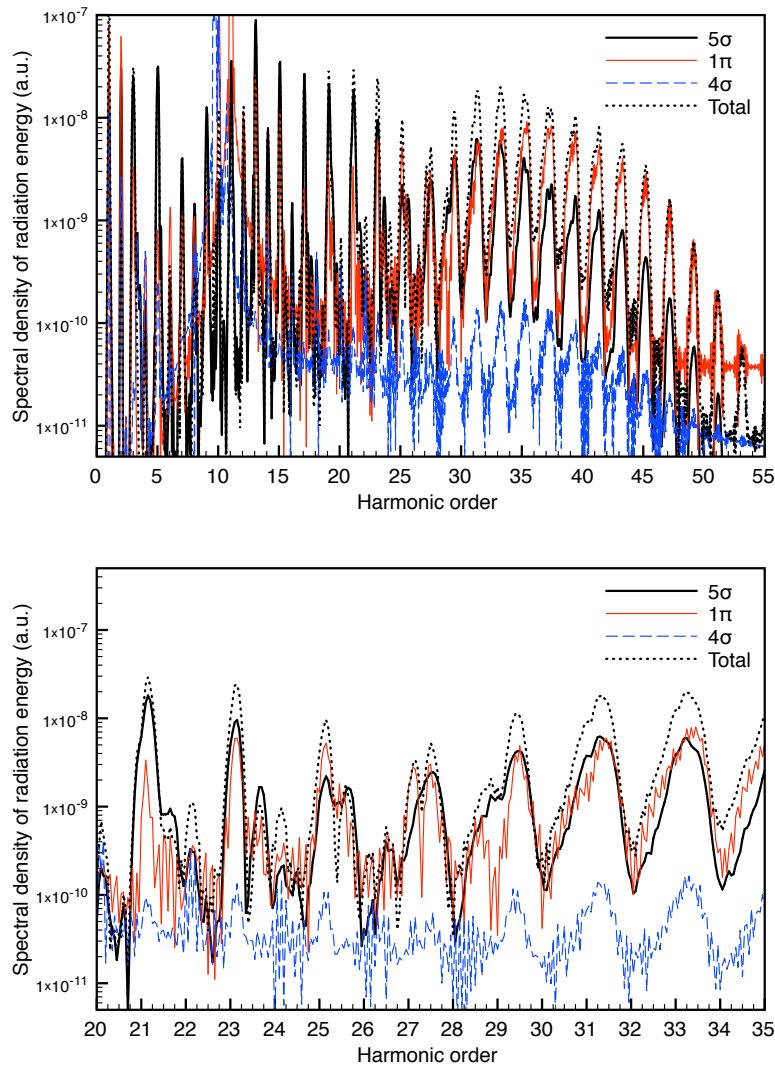


FIG. 23: Total (black dotted line) and orbital ( $5\sigma$  (black line),  $1\pi$  (red line), and  $4\sigma$  (blue dashed line)) harmonic power spectra of the CO molecule in the  $\sin^2$  laser pulse with a peak intensity of  $I_0 = 3 \times 10^{14} \text{ W/cm}^2$ . The laser pulse has a wavelength of 800 nm and a time duration of 20 optical cycles: orientation angle  $\gamma = 90^\circ$ .

of many-electron quantum molecular systems in the presence of intense ultrashort laser fields. They allow the construction of orbital-independent single-particle local exchange-correlation potential which possesses the correct  $(-1/r)$  long-range asymptotic behavior. With the asymptotically correct potential, the energy of the highest occupied spin-orbital provides a good approximation to the ionization potential. The generalized pseudospectral

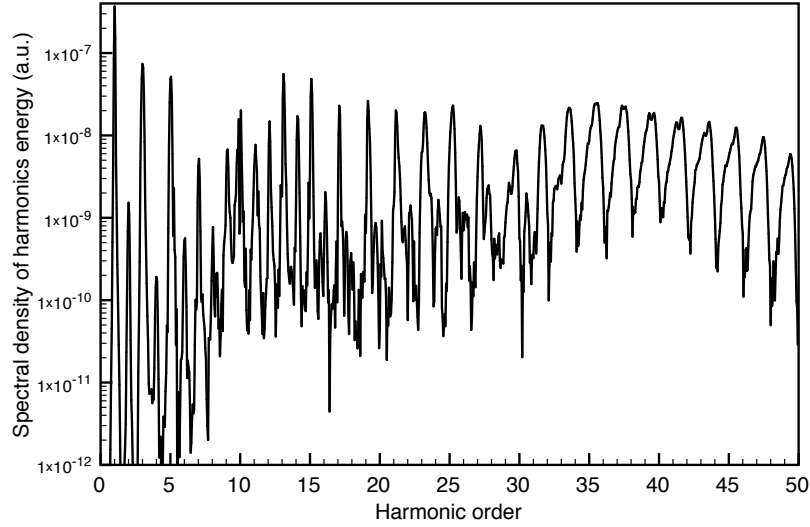


FIG. 24: Total harmonic power spectra of the CO molecule in the  $\sin^2$  laser pulse with a peak intensity of  $I_0 = 4 \times 10^{14}$  W/cm<sup>2</sup>. The laser pulse has a wavelength of 800 nm and a time duration of 20 optical cycles: orientation angle  $\gamma = 90^\circ$ .

(GPS) technique allows the construction of non-uniform and optimal spatial grids, denser mesh nearby each nucleus and sparser mesh at longer range, leading to high-precision solution of both electronic structure and time-dependent quantum dynamics with the use of only a modest number of spatial grid points. The TDDFT formalism along with the use of the time-dependent GPS numerical technique provides a powerful new nonperturbative time-dependent approach for exploration of the electron correlation and multiple orbitals effects on strong field multiphoton processes.

Like the steady-state case, the exact form of time-dependent xc energy functional is unknown. Most of the strong-field calculations so far (including those discussed in this chapter) have used the *adiabatic* approximation, neglecting the memory-effect terms in the xc potential. As shown by the recent study [98], the adiabatic approximation is well justified in the case of medium-strong low-frequency laser fields. However, its validity in very strong fields still remains to be investigated. More rigorous nonadiabatic treatment of the time-dependent xc energy functional can be facilitated if some information regarding the electron density for  $N$ -electron systems can be determined by means of the fully *ab initio* wavefunction approach. But this task is not feasible at the current time for  $N > 2$ . Since the exact time-dependent xc energy functional form is supposed to be universal and independent of  $N$ , the information of the strong-field behavior of the simplest but nontrivial two-electron systems will be very valuable for the future construction of time-dependent xc energy functional.

Applicability of the modern TDDFT approaches for the treatment of multiple elec-

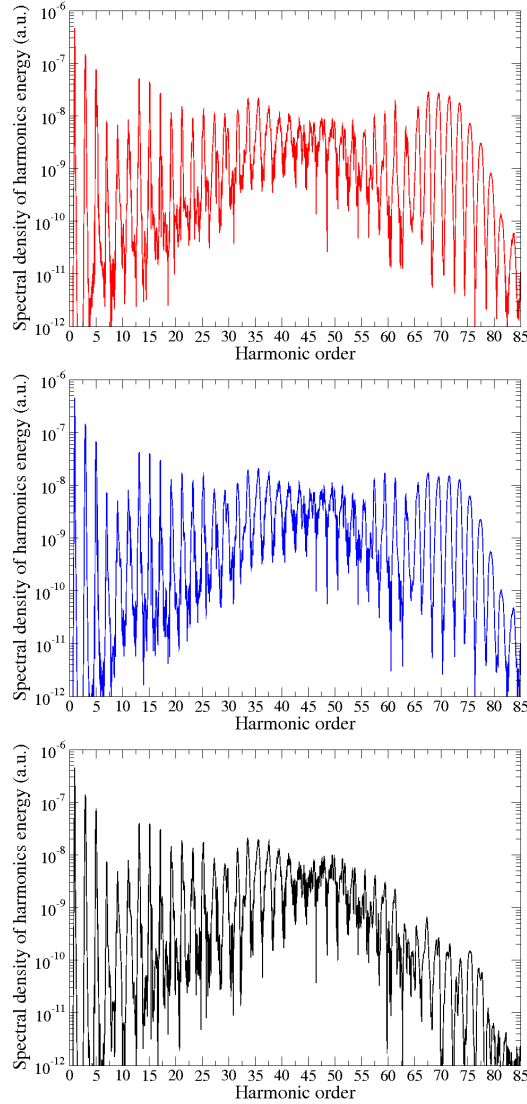


FIG. 25: Total harmonic power spectra of the CO molecule in the  $\sin^2$  laser pulse with a peak intensity of  $I_0 = 5 \times 10^{14}$  W/cm<sup>2</sup>. The laser pulse has a wavelength of 800 nm and a time duration of 20 optical cycles: orientation angle  $\gamma = 80^\circ$  (red line); orientation angle  $\gamma = 85^\circ$  (blue line); orientation angle  $\gamma = 90^\circ$  (black line).

tron ionization processes is another problem related to the quality of time-dependent xc energy functionals. Most of approximate xc functionals lack the important property of the exact functional, the discontinuity of its derivative with respect to the number of particles  $N$ , when  $N$  passes through integer values [99]. Several attempts to apply TDDFT with such approximate functionals for calculations of nonsequential double ionization were un-

successful [100, 101]. Recently it was shown [102] that the derivative discontinuity is crucial for correct description of double ionization. The TD-OEP/KLI-SIC xc potential possesses an integer discontinuity with respect to the *spin* particle number  $N_\sigma$  which improves description of the ionization process. However, we have found [103] that such a discontinuity of the TD-KLI-SIC potential is not sufficient to reproduce characteristic features of double ionization. However, when an integer discontinuity is enforced with respect to the *total* particle number  $N$ , the famous “knee” structure, experimentally observed in double ionization of He atoms, can be reproduced in TDDFT calculations [104].

At this time, the TDDFT is the primary approach available for the nonperturbative treatment of time-dependent processes of many-electron quantum systems in strong fields. Further extension of the *self-interaction-free* TDDFT approaches to larger molecular systems will be valuable and can lead to significant advancement in the understanding of strong-field chemical physics and atomic and molecular physics in the future. Work in this direction is under progress.

## Acknowledgments

This work was partially supported by National Science Council of Taiwan and National Taiwan University (Grant No. 102R104021 and 102R891401). D.A.T. acknowledges the partial support of St. Petersburg State University (Grant No. 11.38.654.2013).

## References

- [1] F. Krausz and M. Ivanov, *Rev. Mod. Phys.* **81**, 163 (2009).
- [2] Z. Chang, *Fundamentals of Attosecond Optics, 1st ed.* (CRC, Boca Raton, 2011).
- [3] Z. Chang, *J. Opt. Soc. Am. B* **27**, 9 (2010).
- [4] G. Sansone, E. Benedetti, F. Calegari, C. Vozzi, L. Avaldi, R. Flammini, L. Poletto, P. Villoresi, C. Altucci, R. Velotta, et al., *Science* **314**, 443 (2006).
- [5] E. Gustafsson, T. Ruchon, M. Swoboda, T. Remetter, E. Pourtal, R. López-Martens, P. Balcou, and A. L’Huillier, *Opt. Lett.* **32**, 1353 (2007).
- [6] K. Zhao, Q. Zhang, M. Chini, Y. Wu, X. Wang, and Z. Chang, *Opt. Lett.* **37**, 3897 (2012).
- [7] M. Hentschel, R. Kienberger, C. Spielmann, G. A. Reider, N. Milosevic, T. Brabec, P. Corkum, U. Heinzmann, M. Drescher, and F. Krausz, *Nature* **414**, 509 (2001).
- [8] A. Baltuška, T. Udem, M. Uiberacker, M. Hentschel, E. Goulielmakis, C. Gohle, R. Holzwarth, V. S. Yakovlev, A. Scrinzi, T. W. Hänsch, et al., *Nature* **421**, 611 (2003).
- [9] R. Kienberger, M. Hentschel, M. Uiberacker, C. Spielmann, M. Kitzler, A. Scrinzi, M. Wieland, T. Westerwalbesloh, U. Kleineberg, U. Heinzmann, et al., *Science* **297**, 1144 (2002).
- [10] S. Baker, J. S. Robinson, C. A. Haworth, H. Teng, R. A. Smith, C. C. Chirilă, M. Lein, J. W. G. Tisch, and J. P. Marangos, *Science* **312**, 424 (2006).
- [11] M. Uiberacker, T. Uphues, M. Schultze, A. J. Verhoef, V. Yakovlev, M. F. Kling, J. Rauschenberger, N. M. Kabachnik, H. Schröder, M. Lezius, et al., *Nature* **446**, 627 (2007).
- [12] M. Drescher, M. Hentschel, R. Kienberger, M. Uiberacker, V. Yakovlev, A. Scrinzi, T. West-

- erwalbesloh, U. Kleineberg, U. Heinzmann, and F. Krausz, *Nature* **419**, 803 (2002).
- [13] J. Itatani, J. Levesque, D. Zeidler, H. Niikura, H. Pépin, J. C. Kieffer, P. B. Corkum, and D. M. Villeneuve, *Nature* **432**, 867 (2004).
  - [14] See, for example, E. Goulielmakis, Z.-H. Loh, A. Wirth, R. Santra, N. Rohringer, V. S. Yakovlev, S. Zherebtsov, T. Pfeifer, A. M. Azzeer, M. F. Kling, et al., *Nature* **466**, 739 (2010).
  - [15] T. Popmintchev, M.-C. Chen, D. Popmintchev, P. Arpin, S. Brown, S. Ališauskas, G. Andriukaitis, T. Balčiunas, O. D. Mücke, A. Pugzlys, et al., *Science* **336**, 1287 (2012).
  - [16] L. V. Keldysh, *Sov. Phys. JETP* **20**, 1307 (1965).
  - [17] J. Muth-Böhm, A. Becker, and F. H. M. Faisal, *Phys. Rev. Lett.* **85**, 2280 (2000).
  - [18] H. R. Reiss, *Phys. Rev. A* **22**, 1786 (1980).
  - [19] M. V. Ammosov, N. B. Delone, and V. P. Krainov, *Sov. Phys. JETP* **64**, 1191 (1986).
  - [20] X. M. Tong, Z. X. Zhao, and C. D. Lin, *Phys. Rev. A* **66**, 033402 (2002).
  - [21] See, for example, K. C. Kulander, K. J. Schafer, and J. L. Krause, *Time-dependent studies of multiphoton processes in Atoms in Intense Laser Fields*, Adv. At. Mol. Opt. Phys. Suppl. Vol. 1 (Academic Press, Boston, 1992).
  - [22] K. C. Kulander, *Phys. Rev. A* **38**, 778 (1988).
  - [23] P. Hohenberg and W. Kohn, *Phys. Rev.* **136**, B864 (1964).
  - [24] W. Kohn and L. J. Sham, *Phys. Rev.* **140**, A1133 (1965).
  - [25] R. G. Parr and W. Yang, *Density-Functional Theory of Atoms and Molecules* (Oxford University Press, Oxford, 1989).
  - [26] A. D. Becke, *Phys. Rev. A* **38**, 3098 (1988).
  - [27] C. Lee, W. Yang, and R. G. Parr, *Phys. Rev. B* **37**, 785 (1988).
  - [28] J. P. Perdew and Y. Wang, *Phys. Rev. B* **33**, 8800 (1986).
  - [29] J. P. Perdew, K. Burke, and M. Ernzerhof, *Phys. Rev. Lett.* **77**, 3865 (1996).
  - [30] S. I. Chu, *J. Chem. Phys.* **123**, 062207 (2005).
  - [31] X. M. Tong and S. I. Chu, *Phys. Rev. A* **55**, 3406 (1997).
  - [32] R. T. Sharp and G. K. Horton, *Phys. Rev.* **90**, 317 (1953).
  - [33] J. D. Talman and W. F. Shadwick, *Phys. Rev. A* **14**, 36 (1976).
  - [34] J. B. Krieger, Y. Li, and G. F. Iafrate, *Phys. Lett. A* **146**, 256 (1990).
  - [35] J. B. Krieger, Y. Li, and G. F. Iafrate, *Phys. Rev. A* **45**, 101 (1992).
  - [36] T. Grabo and E. K. U. Gross, *Chem. Phys. Lett.* **240**, 141 (1995).
  - [37] A. A. Radzig and B. M. Smirnov, *Reference Data on Atoms and Molecules* (Springer, Berlin, 1985).
  - [38] W. F. Chan, G. Cooper, X. Gao, and C. E. Brion, *Phys. Rev. A* **45**, 1420 (1992).
  - [39] K. Colding, R. P. Madden, and D. L. Ederer, *Phys. Rev.* **155**, 26 (1967).
  - [40] X. M. Tong and S. I. Chu, *Phys. Rev. A* **57**, 855 (1998).
  - [41] K. D. Sevier, *At. Data Nucl. Data Tables* **24**, 323 (1979).
  - [42] X. M. Tong and S. I. Chu, *Phys. Rev. A* **57**, 452 (1998).
  - [43] X. M. Tong and S. I. Chu, *Chem. Phys.* **217**, 119 (1997).
  - [44] X. M. Tong and S. I. Chu, *Phys. Rev. A* **64**, 013417 (2001).
  - [45] J. J. Carrera and S. I. Chu, *Phys. Rev. A* **79**, 063410 (2009).
  - [46] X. Chu and S. I. Chu, *Phys. Rev. A* **63**, 023411 (2001).
  - [47] J. Heslar, J. J. Carrera, D. A. Telnov, and S. I. Chu, *Int. J. Quant. Chem.* **107**, 3159 (2007).
  - [48] S. K. Son and S. I. Chu, *Chem. Phys.* **366**, 91 (2009).
  - [49] S. K. Son and S. I. Chu, *Phys. Rev. A* **80**, 011403(R) (2009).
  - [50] D. A. Telnov and S. I. Chu, *Phys. Rev. A* **76**, 043412 (2007).
  - [51] D. A. Telnov and S. I. Chu, *Phys. Rev. A* **71**, 013408 (2005).

- [52] X. Chu and S. I. Chu, Phys. Rev. A **64**, 063404 (2001).
- [53] M. Abramowitz and I. Stegun, eds., *Handbook of Mathematical Functions* (Dover, New York, 1965).
- [54] L. Tao, C. W. McCurdy, and T. N. Rescigno, Phys. Rev. A **79**, 012719 (2009).
- [55] C. C. Marston and G. G. Balint-Kurti, J. Chem. Phys. **91**, 3571 (1989).
- [56] D. A. Telnov and S. I. Chu, Phys. Rev. A **80**, 043412 (2009).
- [57] D. A. Telnov and S. I. Chu, Comp. Phys. Comm. **182**, 18 (2011).
- [58] X. Chu and S. I. Chu, Phys. Rev. A **63**, 013414 (2001).
- [59] M. R. Hermann and J. A. Fleck, Phys. Rev. A **38**, 6000 (1988).
- [60] M. D. Feit, J. A. Fleck, Jr., and A. Steiger, J. Comput. Phys. **47**, 412 (1982).
- [61] M. A. L. Marques, C. A. Ullrich, F. Nogueira, A. Rubio, K. Burke, and E. K. U. Gross, eds., *Time-Dependent Density Functional Theory* (Springer, Berlin, 2006).
- [62] R. van Leeuwen and E. J. Baerends, Phys. Rev. A **49**, 2421 (1994).
- [63] K. P. Huber and G. Herzberg, *Molecular spectra and molecular structure. IV. Constants of diatomic molecules* (Van Nostrand Reinhold, New York, 1979).
- [64] M. Lein, N. Hay, R. Velotta, J. P. Marangos, and P. L. Knight, Phys. Rev. A **66**, 023805 (2002).
- [65] P. B. Corkum, Phys. Rev. Lett. **71**, 1994 (1993).
- [66] R. D. Nelson, Jr., D. R. Lide, and A. A. Maryott, A. A. *National Standard Reference Data Series Natl. Bur. Stand. (U.S.) Circ. No. 10* (US GPO, Washington, DC, 1967).
- [67] P. R. T. Schipper, O. V. Gritsenko, S. J. A. van Gisbergen, and E. J. J. Baerends, J. Chem. Phys. **112**, 1344 (2000).
- [68] X. Chu and S. I. Chu, Phys. Rev. A **70**, 061402(R) (2004).
- [69] K. Siegbahn, J. Electron Spectrosc. Relat. Phenom. **5**, 3 (1974).
- [70] G. Johansson, J. Hedman, A. Berndtsson, M. Klasson, and R. Nilsson, J. Electron Spectrosc. Relat. Phenom. **2**, 295 (1973).
- [71] H. Hamnett, W. Stoll, and C. E. Brion, J. Electron Spectrosc. Relat. Phenom. **8**, 367 (1976).
- [72] D. W. Turner, C. Baker, A. D. Baker, and C. R. Brundle, *Molecular photoelectron spectroscopy* (Wiley, London, 1970).
- [73] X. M. Tong and S. I. Chu, Phys. Rev. A **61**, 021802(R) (2000).
- [74] M. Leibscher, I. S. Averbukh, and H. Rabitz, Phys. Rev. A **69**, 013402 (2004).
- [75] H. Stapelfeldt and T. Seideman, Rev. Mod. Phys. **75**, 543 (2003).
- [76] D. Pinkham and R. R. Jones, Phys. Rev. A **72**, 023418 (2005).
- [77] D. Pinkham, K. E. Mooney, and R. R. Jones, Phys. Rev. A **75**, 013422 (2007).
- [78] T. Kreibich, M. Lein, V. Engel, and E. K. U. Gross, Phys. Rev. Lett. **87**, 103901 (2001).
- [79] J. Heslar, D. A. Telnov, and S. I. Chu, Phys. Rev. A **83**, 043414 (2011).
- [80] A. Lofthus and P. H. Krupenie, J. Phys. Chem. Ref. Data **6**, 113 (1977).
- [81] R. B. Caton and A. E. Douglas, Can. J. Phys. **48**, 432 (1970).
- [82] D. L. Hildenbrand, Int. J. Mass Spectrom. Ion Phys. **7**, 255 (1971).
- [83] G. Johansson, J. Hedman, A. Berndtsson, M. Klasson, and R. Nilsson, J. Electron Spectrosc. Relat. Phenom. **2**, 295 (1973).
- [84] H. Hamnett, W. Stoll, and C. E. Brion, J. Electron Spectrosc. Relat. Phenom. **8**, 367 (1976).
- [85] D. W. Turner, C. Baker, A. D. Baker, and C. R. Brundle, *Molecular Photoelectron Spectroscopy* (Wiley-Interscience, London, 1970).
- [86] R. W. Shaw and T. D. Thomas, Phys. Rev. A **11**, 1491 (1975).
- [87] D. A. Telnov and S. I. Chu, Phys. Rev. A **79**, 041401(R) (2009).
- [88] A. Lofthus and P. H. Krupenie, J. Phys. Chem. Ref. Data **6**, 113 (1977).
- [89] A. B. Cornford, D. C. Frost, C. A. McDowell, J. L. Ragle, and I. A. Stenhouse, J. Chem.

- Phys. **54**, 2651 (1971).
- [90] K. Siegbahn, C. Nordling, G. Johansson, J. Hedman, P. F. Hedén, K. Hamrin, U. Gelius, T. Bergmark, L. O. Werme, R. Manne, et al., *ESCA Applied to Free Molecules* (North Holland, Amsterdam, 1969).
  - [91] D. Pavičić, K. F. Lee, D. M. Rayner, P. B. Corkum, and D. M. Villeneuve, Phys. Rev. Lett. **98**, 243001 (2007).
  - [92] I. Thomann, R. Lock, V. Sharma, E. Gagnon, S. T. Pratt, H. C. Kapteyn, M. M. Murnane, and W. Li, J. Phys. Chem. A **112**, 9382 (2007).
  - [93] L. D. Landau and E. M. Lifshitz, *The classical theory of fields* (Pergamon Press, Oxford, 1975).
  - [94] B. K. McFarland, J. P. Farrell, P. H. Bucksbaum, and M. Gühr, Science **322**, 1232 (2008).
  - [95] H. J. Wörner, J. B. Bertrand, P. Hockett, P. B. Corkum, and D. M. Villeneuve, Phys. Rev. Lett. **104**, 233904 (2010).
  - [96] A. Etches, M. B. Gaarde, and L. B. Madsen, Phys. Rev. A **84**, 023418 (2011).
  - [97] O. Smirnova, Y. Mairesse, S. Patchkovskii, N. Dudovich, D. Villeneuve, P. Corkum, and M. Y. Ivanov, Nature **460**, 972 (2009).
  - [98] M. Thiele, E. K. U. Gross, and S. Kümmel, Phys. Rev. Lett. **100**, 153004 (2008).
  - [99] J. P. Perdew, R. G. Parr, M. Levy, and J. L. Balduz, Jr., Phys. Rev. Lett. **49**, 1691 (1982).
  - [100] M. Petersilka and E. K. U. Gross, Laser Phys. **9**, 105 (1999).
  - [101] D. G. Lappas and R. van Leeuwen, J. Phys. B **31**, L249 (1998).
  - [102] M. Lein and S. Kümmel, Phys. Rev. Lett. **94**, 143003 (2005).
  - [103] D. A. Telnov, J. T. Heslar, and S. I. Chu, Chem. Phys. **391**, 88 (2011).
  - [104] J. Heslar, D. A. Telnov, and S. I. Chu, Phys. Rev. A **87**, 052513 (2013).